Mixed-metal metal–organic frameworks

Sara Abednatanzi, Parviz Gohari Derakhshandeh, Hannes Depauw, François-Xavier Coudert, Henk Vrielinck, Pascal van Der Voort, Karen Leus

Mixed-metal Metal-Organic Frameworks

Sara Abednatanzi[a,†], Parviz Gohari Derakhshandeh[a,†], Hannes Depauw[a], François-Xavier Coudert[b], Henk Vrielinck[c], Pascal Van Der Voort*[a,d] and Karen Leus*[a]

Mixed-metal MOFs are Metal-Organic Frameworks that contain at least 2 different metal ions as nodes of their frameworks. They are prepared relatively easily by either a one-pot synthesis with a synthesis mixture containing the different metals, or by a post-synthetic ion-exchange method by soaking a monometallic MOF in a concentrated solution of a different (but compatible) metal-ion. More difficult is the accurate characterization of these materials. Is the formed product a mixture of monometallic MOFs or indeed a MOF with different metallic nodes? Are the metals randomly distributed or do they form domains? What is the oxidation state of the metals? How do the metals mutually influence each other, and impact the material's performance? Advanced characterization techniques are required e.g. X-ray absorption spectroscopy, magnetic resonance and electron microscopy. Computational tools at multiple scales are also often applied. In almost every case, a judicious choice of several techniques is required to unambiguously characterize the mixed-metal MOF. Although still in their infancy, several applications are emerging for mixed-metal MOFs, that improve on conventional monometallic MOFs. In the field of gas sorption and storage, especially the stability and affinity towards the target gases can be largely improved by introducing a second metal ion. In the case of flexible MOFs, the breathing behavior, and in particular the pressure at which the MOF opens, can be tailored. In heterogeneous catalysis, new cascade and tandem reactions become possible, with particular focus on reactions where the two metals in close proximity truly form a mixed-metal transition state. The bimetallic MOF should have a clear benefit over a mixture of the respective monometallic MOFs, and bimetallic enzymes can be a huge source of inspiration in this field. Another very promising application lies in the fields of luminescence and sensing. By tuning the lanthanide metals in mixed-metal lanthanide MOFs and by using the organic linkers as antennae, novel smart materials can be developed, acting as sensors and as thermochromic thermometers. Of course there are also still open challenges, as also mixed-metal MOFs do not escape the typical drawbacks of MOFs, such as low stability in moisture and possible metal leaching in liquids. The ease of synthesis of mixed-metal MOFs is a large bonus. In this critical review, we discuss in detail the synthesis, characterization, computational work and applications of mixed-metal MOFs.

1. Introduction

Metal-Organic Frameworks were introduced in the scientific field almost 20 years ago, with the pioneering publications of Yaghi[1] Kitagawa[2] and Férey[3]. Twenty years later the field is still in full expansion. And even up to date one reads in the introduction of many papers that "MOFs are a relatively new class of materials, consisting of inorganic nodes, linked by multifunctional ligands to form highly porous crystalline hybrid materials, finding many applications in catalysis, adsorption, gas storage and sensing". It is indeed strange that MOFs are still experienced and proclaimed as relatively new, while for instance, SBA-15, published by Stucky and Zhao[4] one year earlier (1998) is experienced much more as an "old" material.

MOFs consist of two main components: the organic linkers and the metal inorganic clusters. The linkers act as "struts" that connect the metal ions, which on their part act as "joints" in the resulting MOF architecture. For this reason, the synthesis of MOFs is often based on trial and error techniques. However, the need for "designable MOFs" is high. Within this context, O'Keeffe and Yaghi[5] introduced in 2002 the concept of *isoreticular synthesis* (*iso*: the same, *reticular:* forming a net) which is based on the association of designed rigid secondary building units (SBU) into predetermined ordered structures (networks) which are held together by strong bonds. They illustrated this by reproducing the octahedral inorganic SBU of MOF-5 *by using similar but other* organic linkers.[5] Several functionalities could be easily built into the framework as –Br, –

[a.] *Center for Ordered Materials, Organometallics and Catalysis, Ghent University, Krijgslaan 281-S3, 9000 Gent, Belgium, www.comoc.ugent.be*
[b.] *Chimie ParisTech, PSL University, CNRS, Institut de Recherche de Chimie, Paris, 75005 Paris, France.*
[c.] *Department of Solid State Sciences, Ghent University, Krijgslaan 281-S1, 9000 Gent, Belgium.*
[d.] *Center for Sustainable Chemistry, Ghent University, www.ugent.be/csc*
† Both authors contributed equally to this work
* Corresponding authors: Pascal.Vandervoort@ugent.be; Karen.Leus@ugent.be
Electronic Supplementary Information (ESI) available: literature overview of reported mixed-metal MOFs. See DOI: 10.1039/x0xx00000x

NH_2, $-OC_3H_7$ and $-OC_2H_{11}$. In addition, the pores size could be readily expanded by using elongated organic linkers such as biphenyl, terphenyl and pyrene (Figure 1). This allowed the synthesis of large series of isoreticular MOFs (IRMOFs) in which the functionality could be tuned, and the pore size could be varied from the microporous until the mesoporous range. They were able to increase the pore size from 0.38 nm to 2.88 nm without changing the original topology. The isoreticular principle of Eddaouddi and Yaghi has been cited over 5000 times (at February 2019) and the designability of MOFs has become a major topic. In the fields of catalysis and gas separation, the MOFs are "designed" to have the optimal pore apertures, surface energies, elemental composition for that specific application. Next to isoreticular design, mixing linkers and / or metals are common strategies to tune the properties of the MOFs. The advantages and disadvantages of MOFs are well established by now[6, 7]. The advantages of MOFs are clearly in the first place the high tunability of the materials, in topology, in pore size and in functionalities. The isoreticular chemistry, introduced by Yaghi, offers almost infinite possibilities. In some cases, also the ease of synthesis is a bonus. The most important disadvantages are the use of some unpopular metal ions, such as Cr^{3+}. While Cr^{3+} is not toxic, it is unlikely that companies will want to use it on a large scale due to the strict regulations on storage and disposal of Cr, especially Cr^{6+}. Ironically, the most stable MOF (MIL-101(Cr)) is a Cr-MOF.[7] Because of this, MOFs have found so far most of their applications in the fields of gas storage and gas separation. Many spin-offs and companies are emerging in this field. Research on creating MOFs with multiple functionalities is also a very important field of research with 299 papers in Web of Science in 2018 alone, using the tags Metal, Framework and multifunctional.

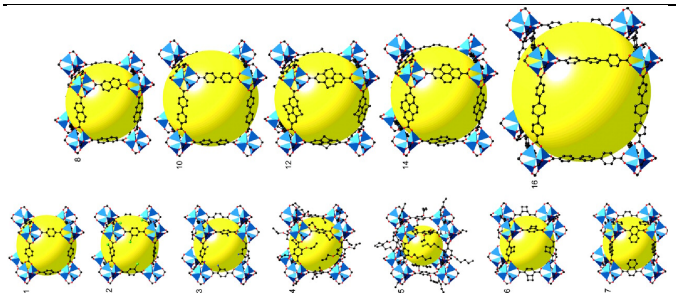

Figure 1: Series of isoreticular Metal-Organic Frameworks based on MOF-5. In IRMOF-1 until IRMOF-7 the organic linker had a different functionality whereas in IRMOF-8 to IRMOF-16, the length of organic linker was changed. Reprinted from ref. [5] with permission. Copyright 2002, American Association for the Advancement of Science.

As one route, materials can be made by a mixed-linker approach in an attempt to introduce multiple functionalities into the same material.[8, 9] Isostructural ligands with different functionalities are required here. Although the principle looks simple, in practice it is often very hard to obtain a nice mixed-linker MOF. Often, in our own experience, the functional groups on the linker will interfere with the coordination to the metal nodes, resulting in an ill-defined, often amorphous material.

One particular example of a mixed-linker MOF that has been frequently used is the well-known UiO-67[10], an isorecticular variant of the UiO-66. UiO-67 is composed of biphenyl-4,4'-dicarboxylic acid (H_2BPDC) linkers that are connected to the $Zr_6(\mu_3\text{-}O)_4(\mu_3\text{-}OH)_4(COO)_{12}$ cluster, giving a three-dimensional face-centered cubic (fcu) network. This framework is interesting due to the possibility to replace the BPDC linker with 2,2'-bipyridine-5,5'-dicarboxylic acid (H_2BPy). The structure of the mixed-linker UiO-67 MOF containing bipyridyl functional groups is shown in Figure 2. This replacement provides an opportunity to the design of the UiO-67(BPy) framework with controlled BPy functional groups for each unit cell.

Moreover, the ability to introduce a large variety of active components, including metal complexes, nanoparticles and organic functional groups into the framework by utilizing the modified ligands directly in the solvothermal synthesis (pre-functionalization) or chemical modification of the framework after synthesis (post-synthetic modification) is an extra advantage to obtain advanced mixed-linker MOF materials suitable for more specialized applications.

Next to the mixed-ligand approach, also the mixed-metal approach, leading to mixed-metal MOFs *(*MM-MOFs*)* is an option to create multiple functionalities. In this review, we will describe the synthesis of such materials, the (often very complicated) analysis of the mixed-metal MOFs, the aid of modelling and typical applications of mixed-metal MOFs in the fields of heterogeneous catalysis, gas sorption, gas separation, luminescence and sensing.

2. Synthetic approaches towards mixed-metal MOFs

The stability of monometallic MOFs is hugely determined by the metal-ligand bond. Bu *et al*.[11] described in a ChemComm review

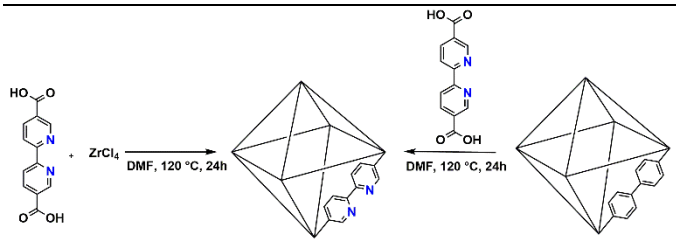

Figure 2: Employed linkers and their assembly into a Zr-based UiO-67(BPy) MOF. The structure is obtainable by one-pot synthesis (left) or by post-functionalization (right). Reproduced from ref. [12] with permission from the Royal Society of Chemistry.

how this interaction can be viewed upon as a simple Lewis acid (metal ion node) – Lewis base (ligand) interaction. The ligands are usually O or N-donors. A strong bond will protect the resulting MOFs against hydrolysis. As a simple rule of thumb, for carboxylic interactions, metals with high charges (typically M^{3+}

or M^{4+}) will form strong Lewis acids that will interact with the strong COO^- Lewis base. On the linker side, a higher stability is obtained if the pK_a of the ligand is increased. This strategy was introduced by Jeffrey Long, and his group that synthesized a pyrazolate MOF (pK_a = 19.8)[13]. The famous ZIFs (Zeolitic Imidazole Frameworks) rely on the same principle, the imidazolate having a pK_a of 18.6. Moreover the dihedral angle closely resembles the siloxane angle, that's why they are referred to as zeolitic frameworks. In an interesting study, Hambley *et al.*[14] analyzed 40000 crystal structures in the Cambridge Structural Database to study the Metal-Ligand covalency from the bonding in carboxylate Ligands. The distinction between an ionic interaction and a covalent interaction is shown in Scheme 1. The distinction between the two interactions can be made by analyzing the two C-O bond lengths. The larger the covalent interaction, the less resonance in the "arms" of the carboxylate group, and the larger the difference in bond lengths between C-O_A and C-O_B. In Figure 3, the % covalency of the metal-carboxylate bondings is shown, as a result of the analysis of 6163 different structures. It is indeed confirmed by this summary that the fraction of covalency increases as the oxidation state of the metal cation increases. For instance, Mn^{2+}-carboxylates have a low fraction of covalency (10%), while Mn^{4+}-carboxylates have a covalency of around 50%. A well-known example is the MIL-101 series, of which the Cr-MIL-101 is one of the most stable MOFs. The same applies to the Zr-based MOFs, built from $Zr_6O_4(OH)_4$ nodes with carboxylate linkers. M^{2+} metals will form unstable structures with carboxylates, i.e. they will degenerate in the presence of water. We refer to our paper that explicitly discusses the stability of some of the most common MOFs[7].

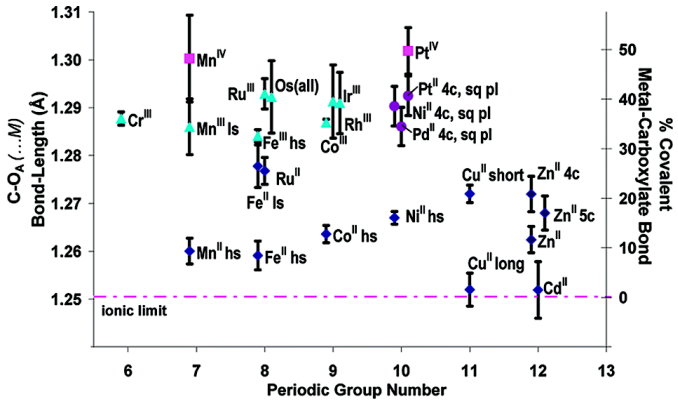

Figure 3: The % covalency of the metal-carboxylate bondings as a result of the analysis of 6163 different structures. Reproduced from ref.[14] with permission. Copyright 2003, the American Chemical Society.

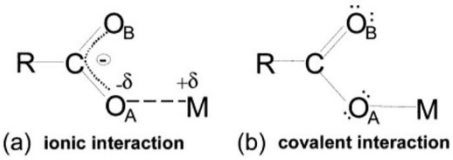

Scheme 1: The distinction between an ionic interaction and a covalent interaction

For mixed-metal MOFs the same principles apply. Replacing (doping) with a less acidic metal ion will destabilize the final product. Moreover, replacing with a less valent ion will result in a charge deficit, that needs to be compensated by exchangeable cations. In addition, one may expect that the size (ionic radius) of the different cations, which is related to their preference to occur in a certain anion coordination[15, 16], also plays a role. In inorganic crystal chemistry ionic radius based considerations are successful in predicting the stability of crystalline phases. An example is the Goldschmidt tolerance factor for crystals with ABX_3 composition (A and B cations, X anion), which has proven able to predict whether or not a cubic perovskite crystal structure will form, and has recently been successfully extended and adapted towards hybrid organic-inorganic perovskites[17-20]. Furthermore it has been observed and calculated that not only charge but also ionic radius (mis)matching determine the preferred dopant lattice site and association to intrinsic (charge compensating) defects in inorganic crystals, e.g. $BaTiO_3$[21, 22]. Similarly, one may expect that large difference in ionic radius may hamper uniform mixing of cations in the SBUs of MOFs and ionic size- and coordination number-related arguments have been invoked to explain why certain ions are more easily accommodated in the SBUs of a MOF structure than others[23].In an excellent review, Cheetham *et al.*[24] explained that Metal-Organic Frameworks should be considered as thermodynamic meta-stable states, as crystal chemistry thermodynamics favor dense structures. However, the thermodynamics and kinetics of forming porous MOFs in solvothermal conditions is still poorly understood.

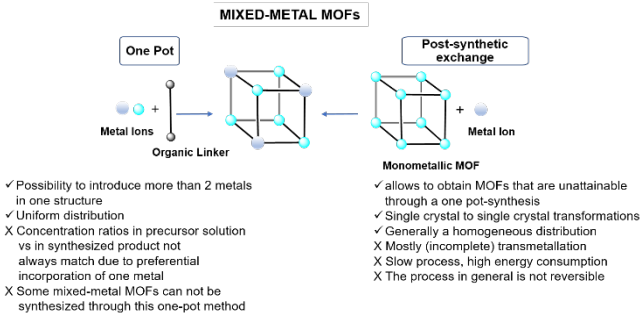

Figure 4: Schematic representation of the possible synthesis routes to prepare MM-MOFs including their advantages and disadvantages.

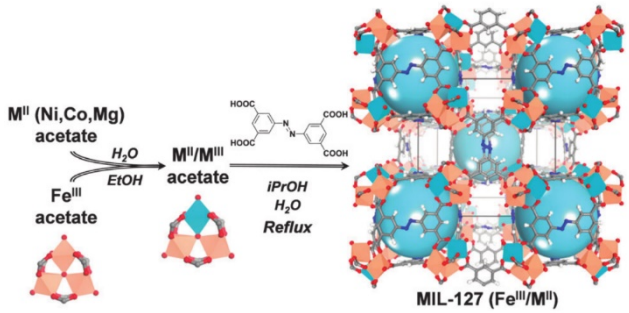

Figure 5: Schematic representation of the SBU approach for the synthesis of mixed-metal MIL-127 materials. Reprinted from ref. [25] with permission from the Royal Society of Chemistry.

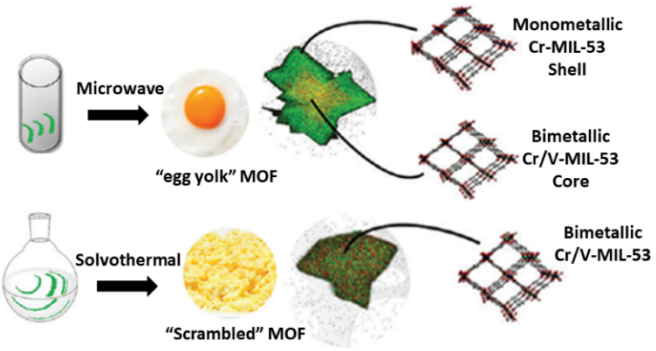

Figure 6: (top) Egg yolk MIL-53 (Cr/V) using the microwave synthesis approach, (bottom) homogeneous dispersion of the metal cations using the solvothermal synthesis route. Reprinted from ref. [27] with permission from the Royal Society of Chemistry.

A further complication is governed by the solvent molecules, that reside inside the MOF cavities and stabilize the structure. Also the autogeneous pressure in the synthesis is considered to be an important parameter in the crystallization of the MOFs. As for MM-MOFs, a deep understanding in the thermodynamics and kinetics of their formation would be highly beneficial and remains a challenge in the years to come. Computer modelling will be a very important asset, as for monometallic MOFs, theoretical calculations can already metastable MOF structures that exceeds the current understanding of crystallization mechanisms.

2.1. Direct synthesis approach or one-pot reaction

MM-MOFs can be prepared by using multiple metal salts as reactants during the conventional solvothermal synthesis, in a one-pot approach (see Figure 4). However, this is not as simple as it sounds. To be able to produce MM-MOFs in a controlled way, it is important to note that the introduced metal cations should react concomitantly to allow a controlled incorporation and to avoid the formation of frameworks based on a single cation. This was for example demonstrated by the group of Serre[26] in which a bimetallic MIL-53 (Cr/Fe) framework was obtained by a direct synthesis. As Cr^{3+} is rather inert while Fe^{3+} is highly reactive, the authors used the less reactive Fe^0 to slow down the reaction of iron-components and to allow a controlled introduction of both metals by controlling the reactivity of the metal ions. Later on, the same group[25] also reported on another strategy to ensure a high control of the metal ratio in MM-MOFs and to obtain frameworks having the envisaged architecture. The authors used the SBU approach to obtain bimetallic MIL-127 materials (Figure 5).

In first instance, neutral mixed acetate building blocks were synthesized having the general formula $Fe^{III}_2M^{II}O(H_2O)_2[O_2C\text{-}CH_3]_6.nH_2O$ with M= Co, Ni or Mg. Hereafter, the obtained metal acetate building blocks were added to the 3,3',5,5'-azobenzenetetracarboxylic acid ligand in a mixture of water and isopropanol for 3 days under reflux. The obtained materials indeed showed a controlled Fe to metal ratio of 2:1. In contrast, the direct synthesis approach using the respective metal chloride salts under similar reaction conditions was unsuccessful and resulted either in amorphous materials or in recrystallized linkers. As environmentally friendly solvents were employed, the authors demonstrated for the first time, the scalable preparation of mixed Fe/Ni, Fe/Co or Fe/Mg MOFs with a space-time yield of about 45 kg m^{-3} d^{-1} (up to 200 g of material could be obtained using a 5 L reactor vessel). Most often the one-pot synthesis strategy results in a more or less homogeneous dispersion of the introduced cations. However, in the study of the group of Van Der Voort [27] it was demonstrated that, depending on the employed synthesis procedure, it was possible to synthesize core-shell heterostructures when the MOFs were synthesized in the kinetic regime. Mixed MIL-53 (Cr/V) structures were prepared either by a solvothermal or a microwave assisted synthesis approach. The X-ray fluorescence (XRF) analysis indicated that vanadium is preferentially introduced into the framework regardless the applied synthesis method. This is due to the fact that the growth rate and nucleation of the V-analogue is significantly higher than that of the Cr-analogue. In addition, the bright-field scanning transmission electron microscopy (BF-STEM) with energy dispersive X-ray (EDX) mapping revealed that the microwave assisted synthesis resulted in "egg yolk" frameworks consisting of a mixed Cr/V core surrounded by a shell which mainly consists of pure MIL-53(Cr). In contrast, the mixed-metal MIL-53 (Cr/V) frameworks obtained through the solvothermal route displayed a homogeneous phase (see Figure 6). The authors suggested that by using a microwave approach, kinetical quenching of the fastest growing component (V) became possible.

Also the group of Walton [28] observed that a difference in crystal growth rate resulted in MM-MOFs having an inhomogeneous distribution of the divalent metal cations. They performed a detailed study to examine the influence of the synthesis temperature and solvent on the final metal composition in Mg/Ni and Mg/Co-MOF-74 materials. All the mixed MOF-74 materials were prepared by a one-pot solvothermal synthesis. The scanning electron microscopy (SEM)/EDX mapping revealed an inhomogeneous metal distribution because of the difference in the crystal growth rate of the mixed MOF-74 materials. In addition, inductively coupled plasma-optical emission spectrometry

(ICP-OES) measurements indicated that Ni and Co were preferentially introduced. The authors observed that the solvent only had a minor influence on the introduced cations whereas the effect of the temperature was more pronounced as the temperature influences the nucleation and the crystal growth. In most cases, 2 metal ions are mixed in one SBU to create bimetallic MOFs however Yaghi and co-workers demonstrated that up to 10 divalent metals could be included in one structure.[23] They reported on the synthesis and characterization of 5 isoreticular microcrystalline MOF-74 structures having 2 (Mg and Co), 4 (Mg, Co, Ni and Zn), 6 (Mg, Sr, Mn, Co, Ni and Zn), 8 (Mg, Ca, Sr, Mn, Fe, Co, Ni and Zn) and 10 (Mg, Ca, Sr, Ba, Mn, Fe, Co, Ni, Zn and Cd) divalent metals within one structure (Figure 7). The multivariate MOFs were obtained through a solvothermal reaction of 2,5-dihydroxyterephthalic acid in the presence of varying amounts of metal salts. The authors observed that there is a preferential incorporation of Mg, Mn, Fe, Co, Ni, Zn and Cd whereas Ca, Sr and Ba are less present because of their tendency to have a higher coordination number (8 instead of 6). However, the authors stated that not only the coordination number but also many other parameters play a crucial role as the final molar ratio of the incorporated metal ions is highly influenced by the pH of the reaction mixture, solubility, reactivity and coordination sphere. In addition, the authors demonstrated that the employed highly reproducible synthesis approach could also be used to introduce metal ions (Ca, Sr, Ba and Cd) from which the parent MOF-74 could not be made directly.

2.2. Post-synthetic exchange

The post-synthetic exchange method allows the formation of frameworks that are difficult or unattainable through a direct synthesis approach (see Figure 4). Up until now, the majority of the reports on post-synthetic modifications dealt with mixed-linkers and only a small number of examples have involved the metal ion exchange to create MM-MOFs. The transmetallation or exchange of the metal nodes typically proceeds by immersing the MOF in a metal ion solution, typically nitrates or chlorides, for several days at room or elevated temperatures to have an (incomplete) transmetallation. Although this post-synthetic exchange procedure is effective, very few studies have investigated the factors that govern the kinetics of this transmetallation. In this context, Lah *et al*.[29] performed an in-depth study to determine which factors influence the kinetics and the thermodynamics of the metal exchange process. They studied the choice of solvent, concentration of the metal ion solution and the exchange temperature. They prepared the Zn analogue of HKUST-1 in which the Zn^{2+} ions were replaced by Cu^{2+} ions by immersing the latter MOF into a $Cu(NO_3)_2.2.5H_2O$ methanol solution at ambient temperature. The authors observed that the transmetallation was incomplete even after soaking the sample for three months. The amount of the replaced framework metal ions (up to 56%) varied – not surprisingly – depending on the concentration of the solution and the time. Also the choice of the solvent was crucial. In addition, the authors synthesized a flexible MOF, denoted as Zn-PMOF-2, having the same $Zn_2(COO)_4$ cluster. Unlike the Zn-HKUST-1, the ICP analysis exhibited complete transmetallation within 3 days soaking the Zn-PMOF-2, even in a lower Cu^{2+} methanol solution. The authors argued that metal centers connected via a flexible organic linker are more reactive than those connected to a rigid organic linker. By reducing the soaking time for the Zn-PMOF-2, a core-shell heterostructure was formed in which the exchange of the framework metal ions occurred selectively at the external shell as these metal centers are more flexible and for this reason are more reactive than those in the internal core. Nevertheless, the reverse transmetallation for both Zn-MOFs was not possible. The first complete and reversible exchange of metal ions within a robust framework via a single crystal to single crystal transformation was reported by Kim and co-workers.[30] They prepared a Cd based MOF having a cubic network. Immersion of this Cd-MOF into an aqueous solution of $Pb(NO_3)_2$ for about one week, resulted in a complete exchange without loss of the single crystallinity. In fact, almost 98% of Cd^{2+} was replaced by Pb^{2+} within only 2 hours. The ion exchange was reversible with retention of the framework. The ICP-atomic emission spectroscopy (AES) analysis revealed that approximately 50% exchange of Pb^{2+} by Cd^{2+} was obtained in 1 day. However, the complete reverse process took almost 3 weeks.

The post-synthetic exchange strategy is also useful to introduce redox active di- and trivalent first row transition metals into MOFs. Among the thousands of reported MOFs none are known to contain for example V^{2+}, as these reduced metal cations (Ti^{3+}, V^{2+}, Cr^{2+}) are incompatible with the typical synthesis conditions of MOFs. Dinca and co-workers[31] demonstrated that the post-synthetic ion metathesis method can be used to introduce V^{2+},Ti^{3+}, Cr^{2+}, Cr^{3+}, Mn^{2+} and Fe^{2+} ions into the MOF-5 host to enable redox reactivity (Figure 8). This was achieved by soaking the MOF-5 crystals in concentrated DMF solutions of $VCl_2(pyridine)_4$, $CrCl_2$, $MnCl_2$ or $Fe(BF_4)_2.6H_2O$ for one week to obtain M-MOF-5 (M= V^{2+}, Cr^{2+}, Mn^{2+} or Fe^{2+}) while $TiCl_3.3THF$,

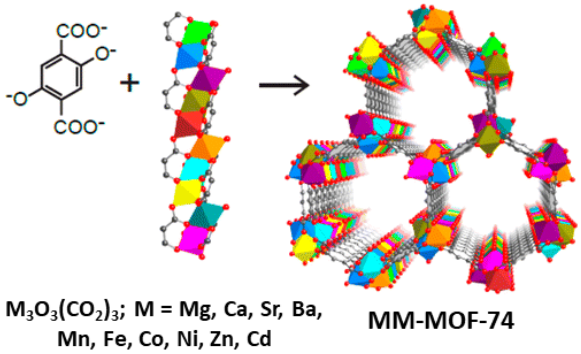

Figure 7: Multivariate MOF-74 materials having up to 10 various metals within their structure. Reproduced from ref. [23] with permission. Copyright 2014, the American Chemical Society.

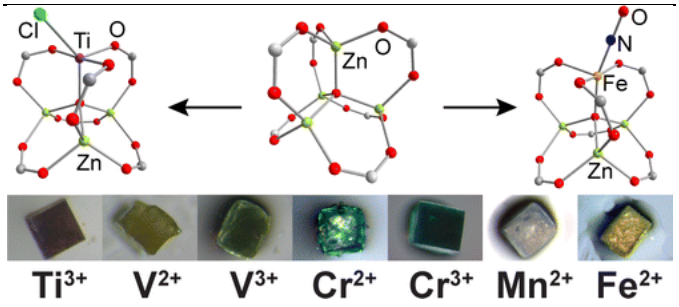

Figure 8: Post-synthetic exchange to introduce reduced metal cations in MOF-5. Reprinted from ref. [31] with permission. Copyright 2013, the American Chemical Society.

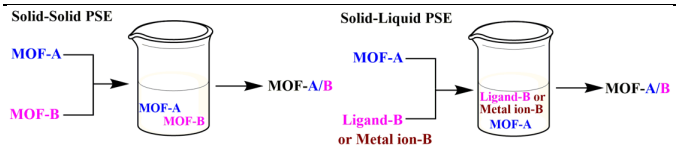

Figure 9: Two possible post-synthetic exchange routes to obtain MM-MOFs: the solid-solid post-synthetic exchange and the solid-liquid post-synthetic exchange. Reproduced from ref. [35] with permission. Copyright 2012, the American Chemical Society.

VCl_3.3THF or $CrCl_3$.3THF was used to introduce Ti^{3+}, V^{3+} or Cr^{3+}. The authors noticed that the degree of exchange after 1 week varied drastically. No equilibrium was reached after 1 week, or in other words, the degree of exchange was kinetically controlled by the stability constants of each substituting cation. The same group also presented a method to determine the thermodynamic parameters of the cation exchange process in MOFs to obtain a better understanding of the mechanistic role of factors such as solvent and cation identity[32]. They concluded that the solvent and cation identity have a significant influence on the equilibrium conditions of the cation exchange for a particular MOF system, while also the thermodynamics significantly alter between different MOFs. The obtained data suggest (not surprisingly) that the post-synthetic cation exchange is an endergonic process requiring a large excess of the metal cations that one wants to exchange to drive the exchange process. In general, the post-synthetic exchange of metal ions is largely focused on less stable MOFs that have labile metal-ligand bonds. However it has also been applied on "inert", highly robust MOFs such as UiO, MIL and ZIF based materials. The first post-synthetic exchange report on chemically and thermally stable ZIF based frameworks was reported by Cohen's group in 2013[33]. In this work the general lability of the metal-nitrogen bonds within ZIF-8 and ZIF-71 having the SOD and RHO topology respectively was demonstrated. More specifically, the redox active transition metal Mn^{2+} was introduced by incubating both ZIF materials in a solution of $Mn(acac)_2$ in MeOH at 55°C during 24 hours. In the exchanged ZIF-71 (Zn/Mn) material almost 12 % of the tetrahedral Zn^{2+} centers were exchanged by Mn^{2+} whereas in the ZIF-8 (Zn/Mn) framework around 10% of the original Zn^{2+} centers were exchanged. In addition, the authors observed that the exchange process could be reversed, or in other words, almost all the Mn^{2+} centers could be exchanged back to Zn. However, attaining a complete metal exchange within these robust MOFs can be cumbersome due to the inertness of the starting metal-ligand bonds. To overcome these limitations, Zhou *et al*. [34] introduced the so called post-synthetic metathesis and oxidation method. In this method a MOF template, denoted as PCN-426-Mg, was chosen having labile metal-ligand bonds. Two possible post-synthetic methods were explored: the direct metathesis and the post-synthetic metathesis and oxidation. In first instance, the trivalent metal ions Fe^{3+} or Cr^{3+} were introduced into the PCN-426-Mg framework by using a direct metathesis in DMF for 12 hours. From the EDX measurements it was observed that 87 % of Fe and only trace amounts of Cr were exchanged. This difference in metal exchange could be explained by the difference in the ligand exchange rate. For Fe^{3+}, the ligand exchange reaction rate constant is around 10^2 k s^{-1} whereas for Cr^{3+} the rate constant is much slower (10^{-6} k s^{-1}). In addition to the incomplete and slow metal exchange rate, framework decomposition was observed during this exchange procedure. To overcome these disadvantages, the authors proposed another post-synthetic metathesis using low-valence but kinetically labile metal ions, followed by an air oxidation to obtain ultra-water stable MOFs. To this end, the solvothermally synthesized PCN-426-Mg was washed with DMF and bubbled with N_2 before the addition of $FeCl_2$ under a nitrogen atmosphere. A complete exchange was observed after 3 hours. Also in the case of $CrCl_2$, a complete exchange was obtained, due to the fact that the Fe^{2+} and Cr^{2+} complexes have a higher stability than that of the Mg^{2+} complex, or in other words, Fe^{2+} and Cr^{2+} have an increased tendency toward complex formation. In a following step, the framework was brought in DMF and bubbled with an air stream to oxidize the Fe^{2+} and Cr^{2+} to Fe^{3+} and Cr^{3+} respectively. Importantly, as Fe^{2+} and Cr^{2+} are softer Lewis Acids in comparison to Fe^{3+} and Cr^{3+}, they interact more weakly with the carboxylate groups, so less destruction of the crystallinity is observed. Both frameworks exhibited an increased stability under acidic and basic conditions as well as a permanent porosity in comparison to the parent PCN-426-Mg as the covalent metal-ligand bond character increased upon increasing the oxidation state of the metal. This corresponds to what has been stated for monometallic MOFs. Another post-synthetic scenario for the exchange of metal ions has been presented by Cohen and co-workers[35], who showed that the metal ion exchange can also occur between two robust MOF solids (Figure 9). They mixed MIL-53 (Al)-Br and MIL-53 (Fe)-Br as dry solids and incubated them in water for 5 days at 85°C. Afterwards, positive-ion aerosol time-of-flight mass spectrometry (ATOFMS) spectra demonstrated that approximately 40% of the

particles contained both Fe and Al and all negative-ion spectra showed the presence of bromide ions which can be assigned to the presence of the Br-BDC ligands. In addition, the authors explored the solid-liquid cation exchange method to enable the formation of new MM-MOFs that could not be attained by the direct solvothermal synthesis method. The introduction of Ti^{4+} cations into the UiO-66 was chosen as objective as Ti^{4+} is not known to form the SBU metal cluster present in UiO-66. Hence, the UiO-66 material was exposed to DMF solutions of several Ti^{4+} salts such as $TiCp_2Cl_2$, $TiCl_4(THF)_2$ or $TiBr_4$ for 5 days at 85°C. It was noted that the Ti loading highly depends on the employed metal salt. The lowest Ti loading was obtained when $TiBr_4$ was used as the metal salt, probably due to its high reactivity and instability while the best incorporation was achieved using $TiCl_4(THF)_2$ as metal salt. ICP-MS measurements indicated that more than 90% of the UiO-66 particles contain Ti^{4+} which corresponds to an overall Ti^{4+} loading of about 38 wt%. From the above presented examples, it is clear that the cation exchange by means of post-synthetic strategies have disadvantages, being the high contact times and the unpredictability of the exchange rate. To circumvent these limitations, Zhou Long *et al.*[36] introduced recently the use of a microwave assisted method to prepare MM-MOFs. Again in this work, UiO-66 was chosen as an example to introduce Ti^{4+}. For the preparation of the UiO-66 (Ti/Zr) material, the Ti metal salt, $TiCp_2Cl_2$, and UiO-66 were mixed in DMF. Afterwards the mixture was transferred into a microwave reactor and kept at 120°C during 4 hours. For comparison the UiO-66 (Ti/Zr) was also prepared solvothermally. ICP-OES measurements revealed that the exchange rate reached over 50% after only 4 hours using the microwave assisted method while only 35% of the Zr was replaced by Ti after 2 days using the traditional solvothermal synthesis method.

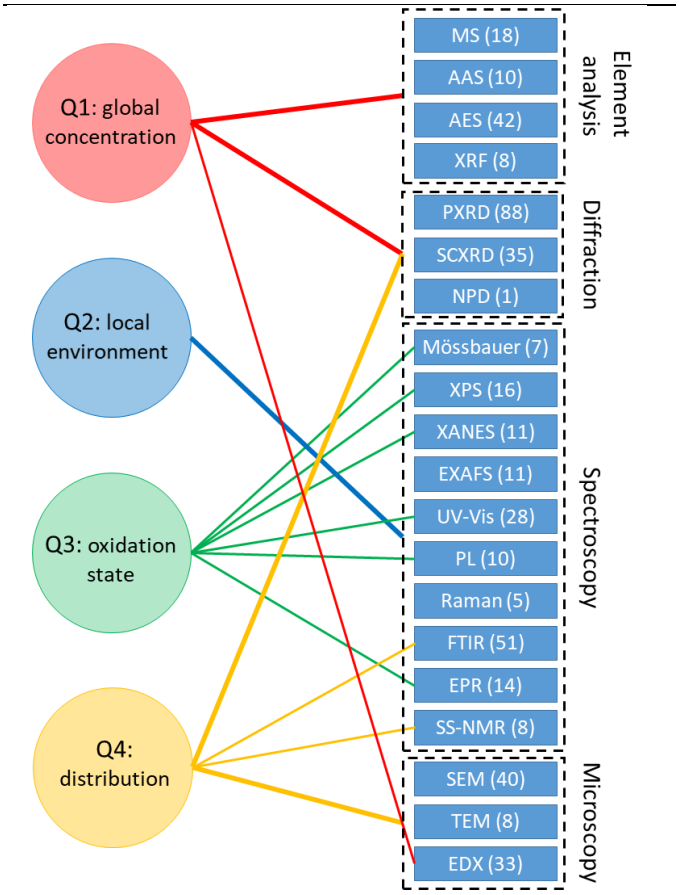

Figure 10: Relation between discussed characterization techniques and MM-MOF specific questions (see text). Numbers between brackets denote the number of papers using this technique in a literature survey of 101 papers. Thin lines connect to one specific techniques and thick lines to a whole group of techniques.

3. Characterization Techniques

Characterizing a MOF involves a combination of techniques to verify whether the anticipated crystalline phase is obtained and whether the framework is properly activated[37]. For a meaningful interpretation of the effects of metal mixing on the properties of MOFs, the used characterization techniques should in addition be able to provide an answer to the following questions:

1) What concentrations of the various metals are actually obtained in the MM-MOF? Do they strongly and (or) systematically differ from the concentrations in the synthesis mixture, in case of one-pot reactions? How do they evolve in transmetallation reactions?

2) What is the location of the metals in the MM-MOF? Are the different metals present as nodes (i.e. incorporated in the framework), or do some end up in the pores or loosely bound to the framework's surface, or even in separate phases?

3) In which oxidation states do the metals occur?

4) How are the different metals distributed in the MOFs? Is a MM-MOF really obtained, or rather a mixture of monometallic MOFs? Are metal concentrations homogeneous over different crystallites in MM-MOF powders and what is the distribution of metals within individual crystallites?

In this section we discuss physicochemical characterization techniques that have the potential to provide direct answers to these questions (and have been used in literature to do so). Therefore, we have chosen to restrict the discussion to spectroscopic and microscopic techniques. This section does not cover techniques like analysis of the thermal stability of MOFs via thermogravimetry (TGA), or porosity and gas sorption characterization, that can provide indirect indications of metal mixing in MOFs, even though these are very relevant in MOFs research and applications.

We have performed a frequency analysis of the spectroscopic and microscopic techniques used in 101 experimental studies of MM-MOFs, and listed the results in Figure 10 and Table S1. Figure 10 relates the characterization techniques with the questions raised above. It should be noted that the application of these techniques in this literature survey was not restricted (and sometimes even not

specifically aiming) to answering questions 1-4 above. The results thus also reflect the popularity of the listed techniques in MOF research in general. The first four chemical analytical techniques in Table S1 aim at determining the global metal concentrations in MM-MOFs (question 1), as will be briefly discussed in Section 3.2. Questions 2 and 3 typically require spectroscopic techniques (entries 8-17 in Table S1), spanning the whole electromagnetic spectrum, from gamma- to radio-waves. Section 3.3 highlights the most appropriate spectroscopic techniques for site identification and oxidation state assessment. Section 3.4 discusses the problem of determining the metal distribution in MM-MOFs. Also here, spectroscopy may provide information, be it on a very local scale. A more global view on the metal distribution within single crystallites and over different crystallites requires microscopic techniques, in most cases electron microscopy, combined with EDX mapping (entries 18-20 in Table S1).

The single most frequently used technique in our survey (Fig. 10, Table S1) is powder X-ray diffraction (PXRD). Also single crystal X-ray diffraction (SCXRD) is very commonly used in this field of research. For this reason, a separate section (Section 3.1) is devoted to these techniques. No single technique in Table S1 is able to provide an unambiguous answer to all four questions. Certain questions are not as straightforward to answer in an unambiguous way as they may seem at first glance. A combination of diffraction, spectroscopic and microscopic techniques is therefore in general required to obtain fairly conclusive answers to the four questions pointed out.

3.1. X-ray diffraction

Powder and single crystal X-ray diffraction are the primary techniques for identifying crystalline phases in MOFs and for determining the crystal structure of new compounds. The X-ray diffraction intensity is determined by the electron density in a crystalline compound. It is therefore not (very) sensitive to light elements (H in particular). Diffraction techniques do not specifically address any of the four questions pointed out, but can be - and have been - used to provide information on metal mixing in MOFs, as explained below.

PXRD is by far the most frequently used characterization technique in Table S1. Specifically in the context of MM-MOFs, the absence of patterns for separate crystal phases is often considered as a first indication of successful metal mixing. PXRD can reveal unwanted phase formation and the occurrence of monometallic instead of MM-MOFs. However, high signal to noise ratio data are required to detect small concentrations of secondary phases. Moreover, the actual contribution of poorly crystallized phases to a mixture of phases may be difficult to assess.[38] In concentration series of MM-MOFs a gradual evolution of the diffraction peak positions between these of the monometallic MOFs is sometimes regarded as a proof of (random) metal mixing, although caution is in order. According to Vegard's law the lattice parameters of alloys and (inorganic) solids state solutions are expected to evolve linearly between the values of the pure solids. However, deviations from such linear relation on the one hand have been interpreted as indications of cluster formation in solid state solutions[39], and on the other they have been predicted to occur for alloy III-V semiconductors[40]. As a clear example of Vegard's law in MM-MOFs, Stock *et al*.[41] found a linear relation between Ce concentration, determined via EDX, and the cubic lattice parameter for a UiO-66 (Zr/Ce) MM-MOF series, as shown in Figure 11. Goodwin *et al*. obtained very similar results for $Zn_{1-x}Cd_x(mIm)_2$ (HmIm = 2-methylimidazole) MM-MOFs.[42] However, in certain cases where monometallic MOFs differ only slightly in lattice parameters, no monotonous relation between the lattice parameters and the metal composition of MM-MOFs has been found[30, 43]. Complete refinement of XRD data should in principle allow to determine the metal composition of MM-MOFs and in case multiple inequivalent metal sites exist, the occupancy with different metals of each of these sites. In practice, however, errors on the analysis, even in SCXRD, may be very considerable. XRD is particularly difficult for discriminating metals that differ only slightly in electron density (Z-number), e.g. within the 3d series. Dinca *et al*. exploited the effect of the anomalous X-ray dispersion near absorption edges on single crystal diffraction to study the site occupancy of 3d metal ions in partially substituted $Mn_3[(Mn_4Cl)_3(BTT)_8]_2$ (BTT= 1,3,5-benzenetristetrazolate). They found that even such advanced analyses are still subjected to considerable uncertainties[44]. Monge *et al*. had to complement SCXRD with neutron powder diffraction (NPD) to resolve the occupancy of the metal sites in Zn-Co MM-MOFs.[45]

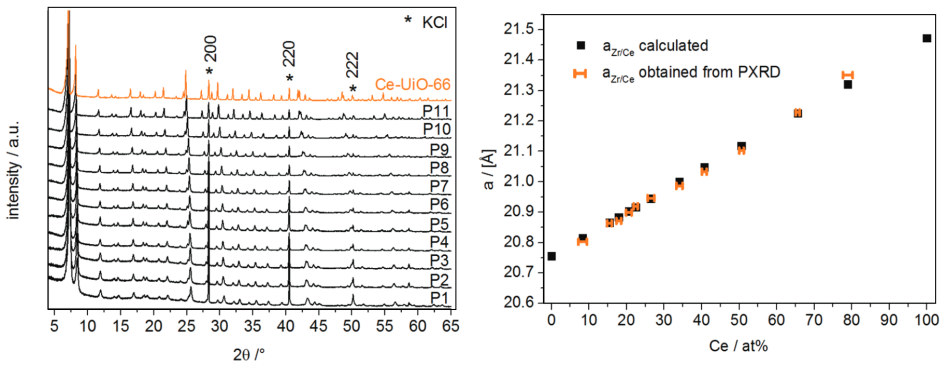

Figure 11: Effect of Ce concentration on the PXRD patterns of UiO-66 (Zr/Ce) and on the cubic lattice parameter extracted from them. Reprinted from ref. [41] with permission from the Royal Society of Chemistry.

Furthermore, even for monometallic MOFs it is not always obvious to distinguish between very similar crystal structures based on XRD results alone. This is nicely illustrated by the fact that NPD[46] and solid state nuclear magnetic resonance (SS-NMR)[47] proved necessary to unveil the fine details of the crystal structure of the dehydrated and hydrated forms of MIL-53(Al), respectively.

3.2. Assessing global metal concentrations

Techniques like flame or ICP atomic absorption spectroscopy (AAS) or AES, and MS are ideally suited to determine absolute element concentrations precisely. They rely on the detection of optical or mass spectra of atoms or small molecular fragments in the gas state. Hence, their main drawback is that they are destructive. XRF can be used as non-destructive alternative, but requires careful calibration. All these techniques provide total, global concentrations of metals in the samples, without spatial resolution, nor information on the location of the metals in the framework. Interestingly, in a few studies of post-synthetic ligand and metal exchange in MOFs from the group of Seth Cohen[35,33] single crystallite elemental analyses were performed by means of ATOFMS, opening perspectives for directly establishing metal mixing in individual crystallites and assessing the homogeneity of metal mixing over different crystallites. X-ray photo-electron spectroscopy (XPS) and EDX are sometimes used to determine the global metal concentrations in MM-MOFs. For XPS the limited information depth of the order of 10s of nm needs to be borne in mind, certainly when comparing with results that follow from bulk analyses. EDX provides elemental composition with a spatial resolution ranging from the nm (coupled to TEM) to the µm scale (SEM). Since only small volumes are probed in this way, data obtained for many positions in the sample should be averaged when measuring global concentrations. An obvious advantage of this approach is that the distribution of the metals over the sample is also assessed (see Section 3.4). Finally, we note that except for XRF, none of the techniques mentioned above are suited for following the metal concentrations *in situ* e.g. during metal exchange reactions. Techniques that allow to determine the metal composition indirectly may offer alternatives in this respect. In their study of the kinetics of post-synthetic metal exchange in Cd-Pb and Cd-Ln MOFs, Kim *et al*. followed SCXRD and PXRD *in situ* during the metal exchange reaction.[30] On a more qualitative level, they also observed gradual color changes in single crystals as a function of metal composition. The optical absorption spectrum in the ultraviolet (UV) – visible (Vis) – near infrared (NIR) region can, indeed, also be used to characterize metal exchange in MOFs, as e.g. illustrated in the work of Zaworotko *et al*.[48]

3.3. Assessing metal incorporation and oxidation state

The oxidation state and molecular environment of a metal ion have an influence on its nuclear and electronic energy levels, as well as on the characteristic vibrational frequencies the metal complex exhibits. This forms the basis of spectroscopic identification of metal sites an oxidation states in MOFs. In the context of proving metal incorporation and mixing in MM-MOFs, spectroscopic techniques should thus be highly sensitive to small changes in the cation environment. In a MM-MOF, both the cations and the organic linkers are expected to occur in a variety of cation environments. This implies that the recorded spectra bear various – possibly partly overlapping – contributions, which renders spectrum analysis difficult and in some cases even impossible. Obviously, this problem is not restricted to MM-MOFs, it quite generally occurs for mixed component, multi-species and disordered systems [49-51]. Moreover, interpretation of spectra is not always unambiguous. Most of the detailed information they contain can only be extracted through spectral fitting and theoretical interpretations (often assisted by first-principles calculations) based on a model of the metal environment. Even though such approach is very powerful, one should bear in mind that the validity of the conclusions is limited by the model space that has been considered.

In spite of these restrictions, various spectroscopic techniques have proven very effective in identifying different metal oxidation states and sites in MOFs, and variations in their environment even as subtle as occupation of pores by different guest molecules. Combining the information that can be obtained from different spectroscopic techniques can lead to very convincing conclusions about the metal location and oxidation state, even if full spectroscopic analysis proves impossible.

The optical absorption and luminescence spectra of main group and transition metal based MOFs in the UV – visible to near IR are most often very broad. Hence, they do not yield very detailed and unambiguous information on metal incorporation, even though spectra may change considerably upon changes in oxidation state and metal exchange. The situation is more favorable for lanthanide ions, where the parity forbidden f-f transitions are narrow and, easily allow to determine the identity and charge state of the ion. Moreover, line positions and occurrence of certain lines are very sensitive to the coordination and symmetry of the lanthanide complex.[52] The luminescence properties of lanthanide MM-MOFs are discussed in Section 7.

The vibrational spectra of MM-MOFs, in most studies probed via FTIR and Raman spectroscopy as a quality check for the synthesis and activation procedures, can also provide proof of

metal incorporation in the SBU of MM-MOFs. In principle, the specific metal-ligand stretch vibrations provide the most direct proof. However, these mostly occur below 600 cm^{-1}, a spectral region that is often not recorded in FTIR spectroscopy. In addition this region is often crowded with deformation modes of the linker molecules and unambiguous identification of these modes often requires first-principles modelling.[53,54] The information provided by these low frequency modes is still underused in MOF research. So far, effects of metal incorporation on the vibrational modes of ligand molecules have proven more effective for establishing metal incorporation and metal mixing.[26] This will be further discussed in Section 3.4.

X-ray absorption techniques are most efficient and generally applicable for determining the metal oxidation state. The sharp edges at the photo-ionization energies of atomic core levels are unique for each atom species and thus provides chemical composition information. Moreover, the edge energy positions are slightly shifted by the oxidation state of the metal and by its chemical binding state. In XPS the energy positions of these edges are measured by analyzing the kinetic energy of the emitted photo-electrons. This limits the information depth to the order of 10 nm, and effectively makes it a surface technique. Moreover, in most setups the experiments need to be carried out under ultrahigh vacuum conditions, incompatible with *in situ* observation of changes in oxidation states under reaction conditions. X-ray absorption edges can also be measured directly either in transmission, or even more sensitively as the excitation spectra of characteristic X-ray fluorescence. The near edge region of this spectrum (XANES= X-ray absorption near edge structure) provides similar oxidation and binding state information as XPS. Even though a complete quantitative analysis of the spectra is very challenging, qualitative features like the upshift of the edge position with increasing oxidation state may be readily interpreted.[51] On certain edges the contributions from different oxidation states are spectrally resolved. Even if this is not the case, determining an average oxidation state for the metal is still possible from the position of the edge. For absolute determination this requires a calibration with compounds for which the oxidation state is known and where the chemical environment of the metal ion is similar to that in the analyzed compound. This is illustrated in Figure 12 a for partially Fe substituted MIL-100(Sc).[55] Regardless of the absolute determination, *in situ* or *ex situ* observation of shifts in the absorption edge position as a result of chemical reactions and thermal treatments can readily be interpreted in terms of an increase or decrease of the average oxidation state. Walton *et al*. used this effect to monitor the Fe^{3+} to Fe^{2+} reduction in MIL-53(Fe) upon insertion of Li^+ (Figure 12 b).[56]

XANES spectra can also reveal information on the symmetry of metal complexes. The occurrence of sharp pre-edge features in the XANES spectra of the first row transition metals indicate strong deviations from inversion symmetry.[51] Analysis of the edge position and pre-edge peak intensity allowed us to follow evolutions in the oxidation state of vanadium dopant ions in MIL-53(Al).[57] The as synthesized MM-MOF exhibited hardly any intensity in the pre-edge region, indicating that most of the V-dopant ions were incorporated as $(V\text{-}OH)^{2+}$ metal nodes which are nearly centrosymmetric. The growth of the pre-edge peak and upshift of the edge position upon solvent extraction and calcination are a clear proof that an important fraction of the dopant is oxidized to $(V{=}O)^{2+}$ by these treatments. This provided an explanation for the growth in intensity of the electron paramagnetic resonance (EPR) spectrum of the paramagnetic $(V{=}O)^{2+}$ ions in these samples upon solvent extraction and calcination. The oscillations in the absorption coefficient farther above the absorption edge find their origin in interference effects in the wave function of the photo-electron that gets scattered by the atoms in the vicinity of the photo-ionized atom[51].

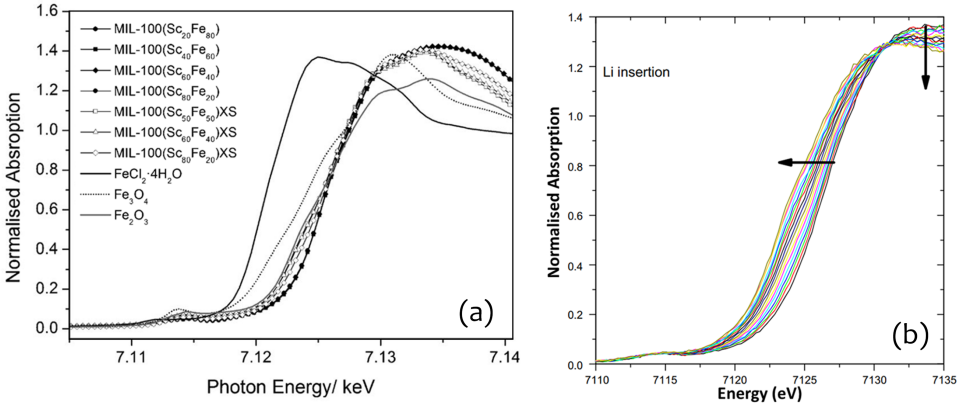

Figure 12: (a) XANES spectra of MIL-100 (Sc/Fe) measured on the Fe K-edge, demonstrating that the dominant Fe oxidation state in the samples is Fe^{3+}, like in Fe_2O_3. Reprinted from ref. [55] with permission. Copyright 2014, John Wiley & Sons, Inc. (b) downshift of the Fe K-edge following the reduction of Fe upon Li^+ insertion in MIL-53(Fe). Reprinted from ref. [56] with permission. Copyright 2009, Elsevier.

Quantitative analysis of EXAFS though fitting provides information on the distance of neighboring atoms, their number and chemical identity.[58] Figure 13 illustrates the power of EXAFS in resolving the tiny shifts in the nearest O-shell distance around Fe in MIL-53(Fe) upon Li^+ insertion.[56] Corresponding changes in the nearest neighboring metal shells proved more difficult to

resolve, though. Similarly, in the study of MM-MIL-53 MOFs EXAFS has proven very effective in determining distances and coordination number in the first coordination shell,[26, 59] providing proof for metal substitution in the metal-inorganic nodes. The EXAFS analysis, however, failed at identifying the ions in the nearest metal shell unambiguously, even for metals as different as Al and Fe. This is probably at least in part due to the composite nature of the spectra as a result of the disorder in the nearest metal ion shells. In contrast, EXAFS analysis of $(Cu_{2.75}Ru_{0.25})_3$-BTC_2 did allow Kleist *et al*. to conclude that Ru^{3+} occurs nearly exclusively in mixed Cu-Ru paddlewheel metal-inorganic units, as expected for random distribution at this low concentration.[60] EXAFS (and XANES) is also quite sensitive in detecting small concentrations of separate metal oxide phases in MOF samples.[55, 59] This is illustrated in Figure 13 b and c, where the Fourier transformed EXAFS spectra for two MIL-100(Sc/Fe) MM-MOFs are compared. One of the samples (c) also contained an α-Fe_2O_3 phase, as confirmed by TEM. The EXAFS spectrum of this sample showed an increased scattering from the nearest cation shell, characteristic for α-Fe_2O_3.

For paramagnetic metal ions EPR spectroscopy can yield very direct and unambiguous proof for incorporation in the framework metal nodes via the detection of hyperfine (HF) interactions with the magnetic nuclei (e.g. ^1H, ^{14}N, ^{27}Al, ^{31}P) in neighboring shells. These small interactions are often not directly observed in the EPR spectra but may be resolved in electron nuclear double resonance (ENDOR) spectra (i.e. NMR for the interacting nuclei detected via intensity changes in the EPR spectra) or various types of HF-sensitive pulsed EPR techniques, e.g. electron spin echo envelope modulation (ESEEM) and hyperfine sublevel correlation spectroscopy (HYSCORE).[61] Figure 14 illustrates this with ENDOR spectra for MIL-53(Al) doped with low concentrations of Cr^{3+} [62] and V^{4+}.[63] HF interactions with the proton of the bridging OH group, with the benzene dicarboxylate protons, and with the ^{27}Al nuclei of the closest neighboring metal shell are observed in the spectra. From the magnitude and anisotropy of these interactions the distance of these nuclei to the paramagnetic ion can be estimated (point dipole interaction). This led to the unambiguous conclusions that $(Cr\text{-}OH)^{2+}$ and $(V{=}O)^{2+}$ substitute regular $(Al\text{-}OH)^{2+}$ framework nodes. Furthermore, the EPR spectra of these paramagnetic probes proved sensitive to transformations of the framework and to the occupation state of the pores.[57, 62, 64, 65]

Frameworks where all metal nodes are occupied with paramagnetic ions, e.g. MIL-47(V), MIL-53(Fe) and $Cu_3(BTC)_2$, yield broad and featureless EPR spectra at room temperature, without resolved HF or other structure.[59, 66, 67] This results from exchange interactions between the paramagnetic ions. At cryogenic temperatures antiferromagnetic ordering occurs, and the broad EPR spectrum strongly decreases in intensity or even vanishes completely. In a couple of studies by Pöppl *et al*. this antiferromagnetic coupling was exploited to obtain narrow-line EPR spectra of Cu^{2+} ions in $Cu_3(BTC)_2$ by mixing in low concentrations (1%) of diamagnetic Zn^{2+} ions.[67, 68] At low temperature only the low concentration of mixed Cu-Zn paddlewheel SBU remained EPR active. EPR combined with ENDOR and HYSCORE then allowed to characterize the interaction of Cu^{2+} in the mixed-metal paddlewheels with CH_3OH[67] and HD gas.[69] The EPR studies mentioned above dealt with low concentrations of paramagnetic ions in diamagnetic MOFs. This is the most favorable condition for obtaining high resolution EPR spectra and sufficiently long spin relaxation times to allow ENDOR and pulsed EPR experiments. All these studies indicated that the dopant ions are dispersed in the framework metal nodes and do not aggregate. It should be noted, though, that aggregates consisting of an even number of paramagnetic ions, that likely couple antiferromagnetically, would remain undetected in EPR spectra.

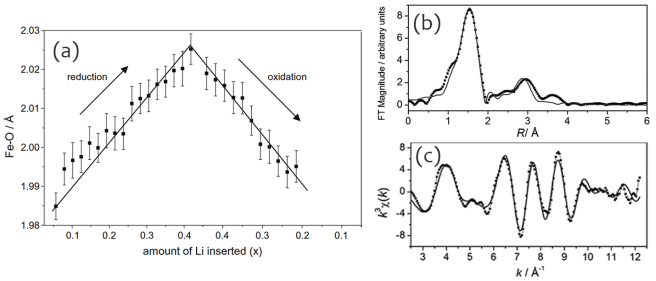

Figure 13: (a) *In situ* EXAFS observation of changes in the average Fe-O distance in the first coordination shell upon Li^+ insertion in MIL-53(Fe). Reprinted from ref. [56] with permission. Copyright 2009, Elsevier, (b) Comparison of the Fourier transform magnitude of the Fe K-edge EXAFS spectra for MIL-100(Sc(0.8)/Fe(0.2)) and (c) for MIL-100(Sc(0.5)/Fe(0.5)) containing also α-Fe_2O_3. Reprinted from ref. [55] with permission. Copyright 2014, John Wiley & Sons, Inc.

Based on the results of EPR, EXAFS-XANES and Mössbauer spectroscopy, Gascon *et al*. suggest that a considerable fraction of the Fe^{3+} dopant ions in MIL-53(Al) are present as antiferromagnetically coupled pairs that are not observed in EPR.[59] A full EPR characterization of Al/V MM-MOFs with the MIL-53 topology (with BDC and NDC linkers)[50] indicated that already at V^{4+} concentrations of about 30% the spectra are dominated by broad features that prevent a detailed analysis of the metal distribution. Our EPR study of the mixed DUT-5(Al) – COMOC-2(V) series (isoreticular with MIL-53, BPDC linkers) indicated that in addition to incorporation at regular framework metal sites, V can also occur in at least one other, as yet not identified site.[70]

EPR is obviously restricted to paramagnetic ions. For diamagnetic ions with nuclear spin, chemical shifts and quadrupole interactions revealed in SS-NMR spectra, may provide similarly detailed information on the metal environment. The SS-NMR spectra of ^{27}Al and $^{69/71}Ga$ in monometallic MIL-53, e.g., proved to be very sensitive to the framework pore state and to the presence of guest molecules

in the pores, e.g. CO_2 and H_2O.[47, 71] In the metal SS-NMR spectra of mixed MIL-53(Al/Ga) MOFs a broadening was observed that reflects the disorder in neighboring cation shells, which was, however, not obvious to interpret in detail.[49] In the same vein, Wright *et al*. found for mixed MIL-100(Sc/Al) MOFs that the ^{45}Sc SS-NMR spectra did reveal the difference between metal-inorganic units with OH and H_2O terminal groups, but did not give direct proof for metal mixing in the trimetallic units.[55] In Section 3.4 the SS-NMR spectra of ligand nuclei, bridging between metal ions will be discussed, which are more sensitive probes for mixing in the SBU's.

For Fe-based MOFs, Mössbauer spectroscopy yields similar structural information as EPR and NMR via isomeric shift, quadrupole and magnetic hyperfine effects on the nuclear transition energy for ^{57}Fe. This gamma-ray technique can in principle also be applied to, e.g. ^{61}Ni, ^{67}Zn and many lanthanide nuclei, but each of these nuclei requires a dedicated radioactive source. In the practice of MOF research Mössbauer spectroscopy has so far been restricted to studies of ^{57}Fe. Based on the recoil-free emission and absorption of gamma-rays by nuclides, spectra are very narrow and well-suited for discriminating and quantifying different sites and oxidation states for Fe. Serre *et al*. studied MIL-53(OH/F)(Fe/Cr) MM-MOFs[26] with Mössbauer spectroscopy, and noticed a marked difference in the quadrupole splitting for Fe^{3+} bridged to neighboring metal ions by OH or F. By quantifying these two contributions in the spectra they established that the Fe ions occupy the OH and F coordinated metal sites randomly. In a recent study, Reguera *et al*. concluded from a Mössbauer analysis that their synthesis procedure for $(Fe,Cu)_3$-BTC_2 did not lead to a MM-MOF, but to separate Cu_3-BTC_2 and Fe_3-BTC_2 phases.[38] Due to poor crystallinity, the diffraction peaks of Fe_3-BTC_2 exhibited considerable broadening, which hampered their detection in the PXRD patterns of the mixture. Mössbauer spectroscopy has proven very effective in detecting the formation of (unwanted) Fe_xO_y phases.[59] The observation of two distinct Fe^{3+} species in the Mössbauer spectra of MIL-53(Al/Fe), but only one isolated Fe^{3+} species with EPR, led Gascon *et al*. to conclude that diamagnetic centers, most probably consisting of neighboring Fe^{3+} ions pairs, occur as important species in these MM-MOFs.[59]

3.4. Assessing the metal distribution

It is clear from the discussion above that determining the location of the metals in MM-MOFs already presents various challenges. Obtaining complete and detailed information on the metal distribution in MM-MOFs, ranging from the distribution over different crystals, over that within single crystals, down to the very local scale of SBUs, presents another important challenge. In a recent study of MOFs with trimeric SBUs and metal porphyrin linkers, with general formula $(M_3O)_2$(TCPP-M)$_3$, Deng *et al*. combined spectroscopic and electron microscopy techniques to study the effect of the metal distribution on the photocatalytic properties of these MOFs.[72] They found SEM-EDX to be very efficient in discriminating between homogeneous mixing and monometallic domain formation in the MOFs, but spectroscopy (in particular XPS) proved necessary to investigate the metal mixing within the trimeric SBUs. Their results indicated that metal mixing in SBUs is essential for obtaining photocatalytic activity exceeding that of mixtures of monometallic MOFs. Since all these levels of the distribution appear relevant for understanding the properties of the MM-MOF, we will first focus attention to microscopic techniques in this section and then discuss successful spectroscopic assessments of metal mixing within the SBUs. In rare cases, optical microscopy can be used to assess the metal distribution in MM-MOF crystallites, as illustrated in the work of Lah *et al*.[29] They studied a post-synthetic transmetallation process in which Cu^{2+} was introduced into $Zn_3(BTC)_2$ in a $Cu(NO_3)_2{\cdot}2.5H_2O$ methanol solution. Crystals of submillimetre size were obtained that changed colour upon Cu-substitution and optical microscopy clearly showed that the metal exchange proceeded from the outer surface of the crystal towards the center. For smaller crystal dimensions electron microscopy becomes necessary. The characteristic X-rays emitted by atoms that get ionized by the incident electron beam can then be used for element analysis (EDX).

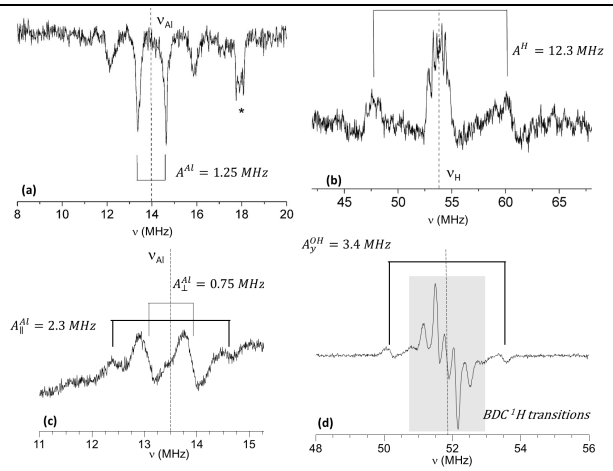

Figure 14: (a) Q-band Mims ENDOR (pulsed, 34 GHz microwave frequency) of MIL-53(Al) doped with 1% Cr^{3+} in the ^{27}Al frequency range, and (b) Davies ENDOR (pulsed, 34 GHz) in the ^1H range of MIL-53(Al) doped with 1% Cr^{3+}. Reprinted from ref. [62] with permission. Copyright 2010, the American Chemical Society. Q-band (34 GHz) CW-ENDOR (frequency modulated) of 1% V-doped as synthesized MIL-53(Al) (c) in the ^{27}Al range and (d) in the ^1H range. Reproduced from ref. [63] with permission. Copyright 2015, John Wiley & Sons, Inc.

Table S1 shows that SEM is frequently used in MM-MOF research, mostly for studying sample morphology and crystallite size, but very often also coupled to EDX element analysis and mapping. The resolution of EDX elemental mapping coupled to SEM largely depends on the interaction volume of the incident electrons with the sample and can go up to several µm. In many studies, EDX metal compositions closely resemble the bulk

compositions (determined by e.g. AES or MS), mapping images suggest a homogeneous distribution over the sample and are not analyzed in great detail. A notable exception is the work of Yaghi *et al*. who studied multivariate MOF-74 samples containing up to 10 different metals, synthesized in a one-pot reaction.[23] Their extensive SEM-EDX analysis revealed considerable inhomogeneity in the metal distribution, even for the binary MOF-74(Co/Mg), as shown in Figure 15. In addition to concentration differences between different crystallites, also variations within crystals were found. Walton *et al*. confirmed these results for MOF-74(Co/Mg) and MOF-74(Ni/Mg) MM-MOF series.[28] These findings underline that inhomogeneity of metal mixing may be an important element in understanding the properties of the MOFs and in theoretical explanations of observed effects.

In general much higher spatial resolution can be obtained when EDX is detected with higher electron energy beams for very thin samples, coupled to STEM. Moreover, STEM offers additional possibilities of (heavy) element discrimination by selectively detecting transmitted electrons at different diffraction angles. We found no use of (high angle) annular dark field STEM in our literature survey of MM-MOFs, though. It should, however, be born in mind that high-energy electron beams can create defects or even structural changes in MOFs[73]. STEM-EDX studies on MM-MOFs are still quite rare, but indispensable for revealing the metal distribution in µm and sub-µm sized MOF crystals. As mentioned earlier, Van Der Voort *et al* exploited the high resolution of STEM-EDX to reveal the egg yolk-like metal distribution within MIL-53(Cr/V) crystals when synthesized via a microwave-assisted reaction (see Figure 6).[27]

In Section 3.3 we have shown that the X-ray, magnetic resonance and Mössbauer spectra of metals in MM-MOFs may be very sensitive to the nearest coordination environment of

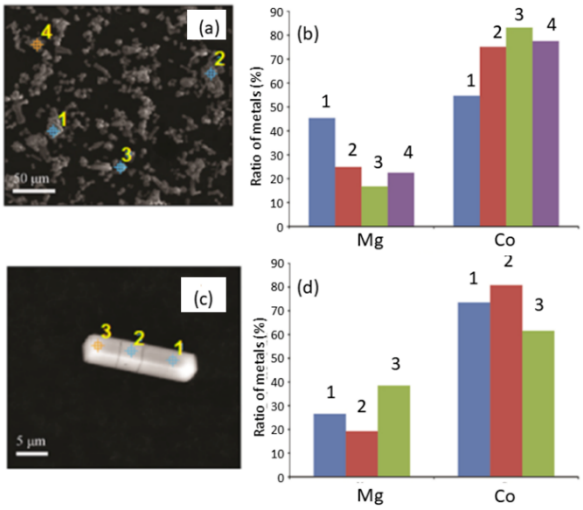

Figure 15: Illustrations of inhomogeneous metal mixing in MOF-74(Co/Mg), as revealed by SEM-EDX, between crystallites ((a) SEM image and (b) EDX point scans on the indicated positions in (a)) and within a crystallite ((c) SEM image and (d) EDX point scans on the indicated positions in (a)) . Reproduced from ref. [23] with permission. Copyright 2014, the American Chemical Society.

the metals, but that disorder in the nearest cation shells is more difficult to resolve, interpret and quantify. Deng *et al*.[72] based their spectroscopic assessment of cation mixing in the SBUs mainly on XPS, but also there the effects were very subtle. A couple of MM-MOF studies indicated that the spectra of the ligands bridging between metal ions in the SBUs are more sensitive probes for metal mixing.

Serre *et al.* found that the frequency of the FTIR active δ-bending mode of the bridging OH in MIL-53(Fe/Cr) is very sensitive to the nearest metal environment (Figure 16 a).[26] The modes of Fe-OH-Fe, Fe-OH-Cr and Cr-OH-Cr moieties were clearly resolved in the FTIR spectra. From the intensities of the corresponding vibrational bands it was concluded that these moieties occur in concentrations as expected for random occupation of the metal nodes by the two metals. More recently, spectral deconvolution of in plane methylimidazolate (mIm=2-methylimidazolate) bending modes in a mixed ZIF-8(Zn/Cd) series of MOFs allowed to conclude that Zn-mIm-Zn and Cd-mIm-Cd moieties occur more frequently than expected for complete random mixing.[42]

Very recently Ashbrook *et al*. reported a cost-effective and atom-efficient method for enriching MOFs in ^{17}O.[49] They applied it to monometallic and MM MIL-53(Al/Ga). In the magic angle spinning SS-NMR spectra the ^{17}O transitions of the carboxylate and hydroxyl groups could be clearly distinguished. The metal environment was found to have a pronounced effect on the quadrupole coupling of the hydroxyl ^{17}O (see Figure 16 c). The decomposition of this region in contributions from Al-OH-Al, Al-OH-Ga and Ga-OH-Ga moieties revealed that the metal distribution was not completely random: pairing of identical ions turned out to be significantly preferred.

4. Computational techniques

In this section, we will focus on the theoretical and computational approaches that have been reported in the literature to study the structure, physical and chemical properties of MM-MOFs. Among the vast body of computational studies on MOFs and coordination polymers in general,[74, 75] published works on MM-MOFs appear relatively few and far between. We can attribute this to the complexity of the mixed-metal systems, both in terms of the experimental characterization necessary to generate structural models, as well as in the modelling approaches themselves. Indeed, the computational cost of modelling techniques in chemistry is dictated by the accuracy of the method employed (quantum chemistry describing electronic degrees of freedom; classical force fields for atomistic descriptions; coarse-grained

simulations), as well as the length and time scales of the phenomena under study.

Contrary to the description of periodic MOF structures with a single metal center, MM-MOFs increase the dimensionality of the problem to be studied and add to the chemical complexity as well. First, they require the study of the system at larger length scales: even for ordered mixed-metal systems, the unit cell is typically a supercell of the monometallic parent. Moreover, in many cases the disposition of metal centers is unknown, or thought to be disordered, and a number of superstructures need to be generated and characterized. Finally, because MM-MOFs involve different types of metal–organic coordinative bonds with rather subtle differences, they need to be described with high-accuracy methods — typically at the quantum chemical level. Thus the detailed description of MM-MOFs is still an open challenge, and a difficult one. We describe below some of the approaches that have been followed to attack it. We also highlight that these challenges (high dimensionality, large length scales, need for an accurate description of weak interactions) are also found in other areas of computational MOF research, and in particular in the characterization of flexibility, defects and disorder.[76]

4.1. Impact on framework properties

The study of the influence of the nature of the metal cations in MOFs is a question that has been raised, from the very early days of the field. There has thus been a large computational effort to address it, for example by systematic studies of the structure and properties of series of isoreticular MOFs with varying metal cations, such as M-IRMOF1 (M = Zn, Cd, Be, Mg, Ca, Sr, Ba).[77, 78]One of these studies, by Widom *al*.[77], was to our knowledge the first to discuss, in addition to the various monometallic IRMOF-1 variants, the effect of doping a framework with a second metal center.

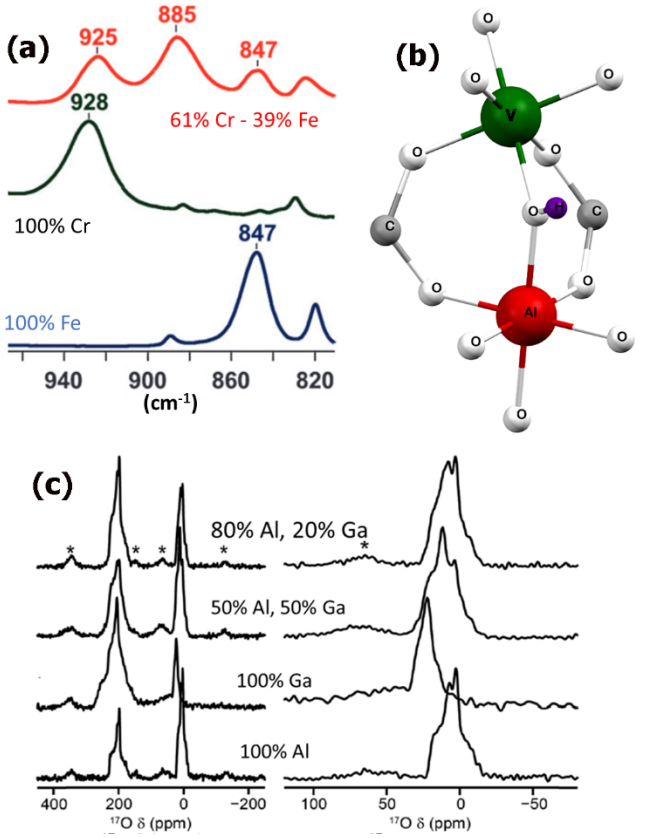

Figure 16: (a) FTIR spectra of MIL-53(Fe/Cr) in the δ-OH bending mode region. Reproduced from ref. [26] with permission from the Royal Society of Chemistry; (b) two neighboring metal nodes in MIL-53; (c) ^{17}O (20.0 T, 16 kHz) spin echo MAS NMR spectra of MIL-53(Al/Ga), full spectra on the left and zoomed in on the hydroxyl region. Asterisks denote spinning sidebands. Reproduced from ref. [49] with permission from the Royal Society of Chemistry.

Using periodic density function theory (DFT) calculations, the authors looked at the impact of substituting one M per unit cell (M = Zn or Be) with a aluminum atom. They showed that the resulting bimetallic MOF had different electronic properties from its parent compound — namely, a smaller band gap. They also demonstrated that a different strategy, adding a lithium atom to the M_4O metal center, on the other hand, induced large structural changes without strongly altering the electronic properties.

Since then, other studies have dug into the question of the electronic properties of MM-MOFs, with the same methodology of DFT calculations. This imposes, of course, a restriction on the nature of the metal centers distribution and concentration, depending on the size of the MOFs' unit cells (or clusters, for non-periodic calculations). For example, working on a cluster composed a single paddle-wheel unit — with two metal atoms — Shustova *et al*.[79] studied the densities of states of Cu–Co–BTC, but were limited to substitution rates of 0 and 50%. Similarly, the study of bimetallic Hofmann-type compounds by

Kang *et al*.[80] was limited, by the high symmetry of the compound, to strictly alternating metal centers in the lattice: they explored the structural, magnetic, and electronic properties of different Hofmann MOFs (Ni–Cr, Ni–Mn, Ni–Fe, Ni–Co). Finally, in 2015, Li *et al*.[81] looked at the effect of Ti doping in NH_2-UiO-66(Zr), and combining DFT calculations with EPR spectroscopy showed that the Ti dopant acts as an electron mediator in promoting the electron transfer, thus enhancing the photocatalytic performance for CO_2 reduction and hydrogen evolution under visible light. This study was limited to doping by one Ti atom in the unit cell (i.e. a 5:1 Zr:Ti ratio).

Finally, we note that although most of the work described above focused on structural and electronic properties, there have also been studies of the impact of mixed-metals in MOFs on their adsorption performance. In a 2013 report, Hill *et al*.[82] described the impact of a Zr → Ti substitution in UiO-66 on its CO_2 adsorption capacity. This study, performed at the classical level using Grand Canonical Monte Carlo and a classical force field for the description of MOF/CO_2 interactions, showed that post-synthetic exchange by Ti in UiO-66(Zr) can almost double the CO_2 uptake, due to smaller pore size and higher adsorption enthalpy. This study, however, is based on an assumption: a random distribution of the two metals among the crystallographic sites — an assumption that has not been validated, experimentally or theoretically. The same limitation is true for the 2017 study by Wang *et al*. [83] reporting on the adsorption capacities of functionalized bimetallic CPM-200 (In/Mg) MOFs.

4.2. Catalytic activity and mechanisms

One of the key potential applications of MOFs in general, and MM-MOFs in particular, is their use as catalysts, and it is therefore not surprising that a large fraction of the computational studies on these systems focused on their catalytic activity and the elucidation of the catalytic mechanisms. We refer here the reader to a recent review of the Gagliardi group on the computational design of functionalized MOF nodes for catalysis,[10] and focus specifically below on MM-MOFs in catalysis. These studies are rather "typical" calculations for catalytic properties, studying possible reaction mechanisms by calculating relative energies for each intermediate and transition state. These calculations are usually performed at the Kohn−Sham density functional theory (KS-DFT) level of theory, in order to describe the reactivity at a relatively low computational cost. They can involve either cluster models of the reactive sites, or fully periodic models.

In 2015, Volkmer *et al.*[84] used DFT calculations to characterize the respective activities of Cu and Co metals centers in mixed-metal Cu-Zn and Co-Zn MOFs, by calculating formation enthalpies and activation energies for the preparation of MFU-4l derivatives by side-ligand exchange reactions. Lan *et al*.[85] in 2018 used cluster-based DFT calculations to characterize bimetallic electrocatalysis in oxygen evolution reaction in a series of trinuclear metal carboxylate clusters $Fe_2M(\mu_3\text{-}O)(CH_3COO)_6(H_2O)_3$ (M = Fe, Co, Ni, Zn). They showed that the introduction of a second cationic species (Co, Ni or Zn) improved the catalytic performance over a purely iron-based material, due to a stronger binding interaction. Other studies have gone beyond the simple characterization and rationalization of existing materials, and attempt to guide the search for novel materials with targeted properties. Two recent studies of computational screening of bimetallic MOFs will highlight this. First, Gagliardi *et al*.[86] screened a series of homo- and heterobimetal-functionalized NU-1000 MOF nodes selected to computationally screen the effect of ancillary metals for C−H bond activation. Correlating activation free energies with various chemical descriptors of the cluster models studied, they showed that transition state C···H (and O···H) bond lengths were reasonable predictors, and that materials combining Cu and Lewis-acidic metals had encouraging properties. Another recent study, by Zhang *et al*.,[85] screened bimetallic M-Cu-BTC MOFs in a two-stage strategy: (i) identifying their ability for CO_2 activation, (ii) perform a full characterization of the mechanisms of CO_2 hydrogenation on the top performers.

In addition to these studies, it is important to note that our field is no longer relying solely on finite-size clusters as models for the reactive centers, but is gradually shifting towards full periodic representations of the frameworks. Two recent examples highlight this recent trend. First is the design, by Gascon *et al*., of a site-isolated MM-MOF for selective methane oxidation.[59] This MIL-53(Al/Fe), synthesized by an electrochemical method, contains atomically dispersed Fe active sites in an aluminum-based framework. The authors used

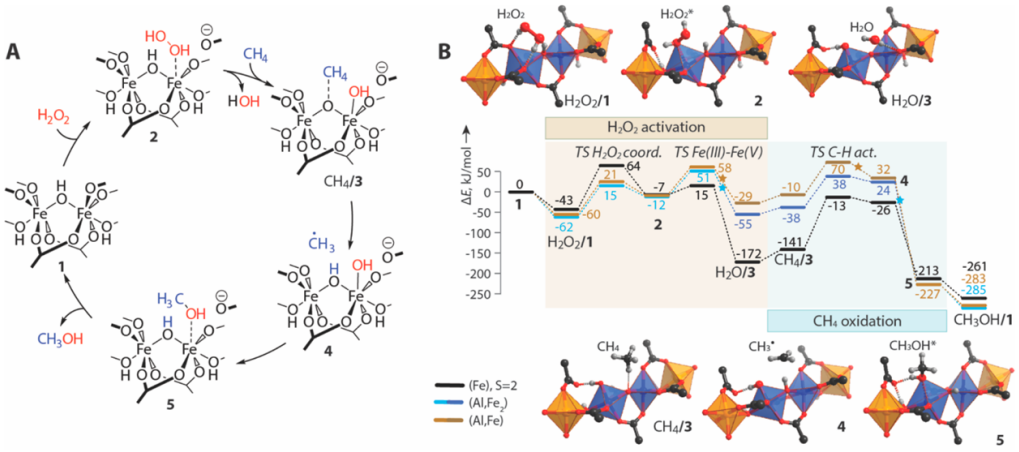

Figure 17: Computational study of methane to methanol oxidation with H_2O_2 over the dimeric Fe site in MIL-53(Al/Fe). A. Proposed mechanism; B. Minimum-energy reaction path diagrams, computed with periodic DFT, (including spin transitions indicated with asterisks) for the catalytic process over different Fe-containing MIL-53 models. Reprinted from ref. [59] with permission. Copyright 2018, the American Chemical Society.

periodic DFT calculations to model the reactivity (methane to methanol oxidation with H_2O_2) on monomeric and dimeric Fe species in the MIL-53(Al) structure.

In order to adequately capture the isolated nature of the sites in a periodic model, they used large supercells of the MOF framework. The proposed reaction mechanism, and the full DFT-computed minimum-energy reaction path diagram associated, are presented in Figure 17. This work was later extended, using the same methodology, considering full reaction network, including formation of the active site, overoxidation of methane to CO_2 and decomposition of H_2O_2 to H_2O and O_2.[59]

Finally, we want to highlight the very recent work of Heinonen *et al*.[87] who went beyond the DFT level of theory, to calculate catalytic energy barriers for ethylene hydrogenation and C–H bond activation in transition-metal-functionalized Zr nodes in NU-1000 using quantum Monte Carlo simulations on clusters. They conclude that, on this realistic cluster model, DFT methods can have errors between 10 and 20 kcal/mol compared to quantum Monte Carlo calculations, shedding some light on the limitations of DFT-based calculations, even with hybrid exchange–correlation functions, for catalytic mechanism studies.

4.3. Distribution of metal centers

Because describing disordered systems is computationally expensive, most of the theoretical studies described above proceed from one of two fundamental assumptions: that the metal centers are either regularly distributed, or randomly distributed. Yet, we know that chemical systems in general, and framework materials in particular, are not always that simple, and solid solutions need not necessarily be fully disordered.[88] In the field of MOFs, this applies as to metal cations as well it does to the linkers, where it was shown for example that UiO-66 materials exhibit correlated disorder in the presence of missing-linker defects[89]— and that this correlated disorder strongly impacts their physical properties.[90] Moreover, the nature of the distribution of metal centers in a heterometallic system is often difficult to probe experimentally, and there is thus a strong need for computational methods that can not only model, but also rationalise, the possible order (or disorder) in metal distributions.

The work by Coudert *et al*.[91] approached this question by borrowing computational tools developed and validated on the study of inorganic solids with substitutional disorder, such as oxide solid solutions and alloys. Focusing on two families of bimetallic MOFs (MOF-5 and UiO-66), Coudert relied on systematic DFT calculations of possible cation distributions at all cation ratios — for a given cell or supercell size. These calculations can predict whether certain metal combinations are expected to lead to solid solution or phase separation, and whether specific geometric arrangements of metal cations are energetically favorable. Overall, bimetallicity is more favorable for pairs of cations with sizes very close to each other, owing to a charge transfer mechanism inside SBUs. In UiO-66, in particular, these authors found that while Zr and Hf cations are expected to form a solid solution, Zr/Ti exchange is not energetically favorable — which is in line with experimental findings.[92]

Another example was a series of two studies by Sholl[93] and Hayes,[94] on the distribution of metals in MM-MOFs MOF-74 (Mg/Ni) and MOF-74 (Mg/Cd), as well as its impact on water and carbon dioxide adsorption. The authors considered a series of metal ion arrangements as a function of composition — although the arrangements considered were not exhaustive — and found that metal mixing was slightly favored over segregation, both energetically and entropically. The impact of bimetallicity on H_2O adsorption was also characterized, but found to be negligible. Beyond bimetallic MOFs, Monge *et al*.[45] reported on a synergistic experimental and computational

study of multication complex arrangements in MOFs with four different metal elements. They used DFT calculations of the formation energy of structures with various cationic configurations, to show that some phases had lower formation energies, which explains the apparition of mesoscale structuration in an Ostwald ripening process that would lead, under thermodynamic control, to complete phase separation.

To finish, we look at one of the most recent and most extensive inquiries in metal centers distribution in MM-MOFs. It is a study by Goodwin *et al*. on the distribution of cations in the compositional family of $Zn_{1-x}Cd_x(mIm)_2$, and its impact on the structure and thermomechanical properties of these zeolitic imidazolate frameworks.[42] Experimental work by the authors determined that there is complete miscibility for all compositions, but that there exist inhomogeneous distributions of Cd and Zn that affect framework apertures. In order to understand the characteristics of the cationic distribution, the authors used reverse Monte Carlo (RMC) modelling to generate atomistic configurations compatible with their experimental infrared spectroscopy data. The authors found that homometallic 4-rings (Zn_4 or Cd_4) are predominant at all compositions — compared to what would be expected from a random Cd/Zn distribution, see Figure 18. There is thus metal clustering, i.e. non-random distribution of metal cations in this ZIF-8/CdIF-1 solid solution. These findings open the way to further tuning of this correlated disorder in MM-MOFs, and therefore have a potential impact on optical, thermal, mechanical, and adsorptive properties of the frameworks. Therefore, the overall efficiency of catalysts both in terms of activity and selectivity can be improved.

5. Mixed-Metal MOFs in Catalysis

Synergistic catalysis is a robust strategy in which the reactants are activated by more than one type of active sites and the reaction energy barrier is significantly reduced.[95]

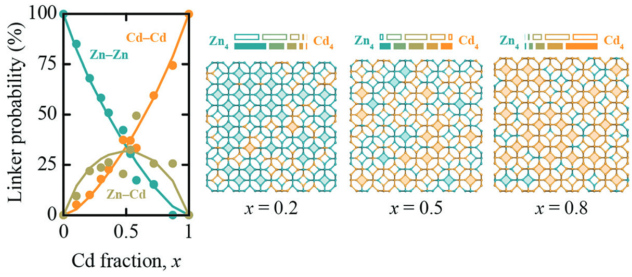

Figure 18: Left: linker probabilities extracted from modelling of the infrared spectroscopy data of fits to the IR data of the ZIF-8/CdIF-1 solid solution. Right: Representative sections of reverse Monte Carlo configurations. Homometallic 4-rings are shaded in teal (Zn) and orange (Cd). The fractional population of Zn_nCd_{4-n} 4-rings is shown in bar representation above each section for (top, open bars) statistical and (bottom, filled bars) experimental distributions. Reprinted from ref. [42] with permission from the Royal Society of Chemistry.

MM-MOFs undoubtedly represent important potential and advantages in synergistic catalysis. One of the main objectives of the development of MM-MOFs is to expand the scope of catalytic reactions with enhanced catalytic performances. Hence, it is necessary to gain a fundamental understanding of the roles of active components and their cooperation to achieve enhanced properties. In this section, selected examples of heterogeneous reactions catalyzed by MM-MOFs and their synergistic effect are described. A full overview of the applied MM-MOFs for a variety of catalytic reactions can be found in Table 1.

5.1. Oxidation Reactions

Selective catalytic oxidation is of industrial importance for fine chemical syntheses[96-98]. Many homogeneous catalysts, often (transition) metal complexes or oxides are still used in some industrial processes[99, 100]. By varying the metal center and the surrounding ligands of these homogeneous catalysts, the chemo-, regio- and stereo-selectivity can be tuned. The metallic sites within MOFs can be employed as active centers for a wide range of heterogeneous catalytic reactions, particularly for oxidations. Within the concept of green chemistry, more efforts should go to performing the oxidation reactions using heterogeneous catalysts with clean oxidants such as air or oxygen. The combination of a heterogeneous metal catalyst with molecular oxygen or air represents one of the best alternatives in the field[101]. M-MOF-74 with the general formula of M_2(DOBDC) (M^{2+}: divalent metal ions; $DOBDC^{4-}$: 2,5-dioxido-1,4-benzenedicarboxylate) is a three-dimensional honeycomb-like network. MOF-74 is a good candidate in oxidation reactions due to its high chemical stability. Additionally, its catalytic activity can be tuned through the replacement of Ni^{2+} in Ni-MOF-74 framework by active Co^{2+} via a post-synthetic metal exchange method.[102] It is interesting to note that Ni-MOF-74 shows almost no activity for cyclohexene oxidation, while its isostructural Co-MOF-74 is active under the same reaction conditions using oxygen as oxidant. With the aim of enhancing the catalytic performance of this framework, the Ni^{2+} ions were substituted partially with the active Co^{2+} ions. The catalytic performance of the partially Co-substituted Ni-MOF-74 (MOF-74 (Co/Ni)) increased with the amount of incorporated Co^{2+}, demonstrating that the incorporated Co^{2+} is serving as the active sites in catalysis (Figure 19). The products observed under the reaction conditions are cyclohexene oxide, 2-cyclohexen-1-ol, 2-cyclohexen-1-one, and cyclohexene hydroperoxide. MOF-74 (Co/Ni) displayed superior catalytic performance even better than pure Co-MOF-74 as Co was placed at positions that were more accessible to the substrate. Additionally, the recycling tests showed no significant loss of the catalytic activity over MOF-74 (Co/Ni) after three reaction runs, exhibiting the overall stability of the material under the reaction conditions. On the other hand, MOF-74 (Cu/Co) with different Cu/Co ratios were obtained via a facile one-pot synthesis method.[103] The bimetallic Cu and Co MOF-74(Cu/Co) catalysts were applied in

the oxidation of styrene using O_2 under solvent-free and mild reaction conditions. The results indicate that not only the styrene conversion over MOF-74 (Cu/Co) but also the selectivity towards benzaldehyde, styrene oxide and phenylacetaldehyde can be tuned by varying the Cu/Co ratio in MOF-74. While MOF-74(Cu) has a very low catalytic activity (0.6% conversion) with 100% selectivity to benzaldehyde, MOF-74(Co) shows higher catalytic activity (47.3% conversion) with a reduced selectivity, resulting in the formation of benzaldehyde, styrene epoxide, phenylacetaldehyde and polystyrene. Interestingly, the incorporation of Cu^{2+} in MOF-74(Co) effectively hinders the polymerization of styrene, however, the incorporation of Co^{2+} in MOF-74(Cu) can improve the conversion of styrene to benzaldehyde, styrene epoxide, and phenylacetaldehyde. The higher activities of MOF-74(Cu/Co) catalysts compared to the physical mixtures of MOF-74(Cu) and MOF-74(Co) with almost the same amounts of Cu and Co proves the synergistic effect of Cu^{2+} and Co^{2+} in the same framework. These studies clearly indicate the superior catalytic activity of mixed-metal MOF-74 over the corresponding single metal MOF, however, the catalysts suffer from serious limitations, like deficient selectivity and conversion with narrow substrate scope.

5.2. Epoxidation Reactions

The selective epoxidation of olefins to the corresponding epoxides is a fundamental transformation both in laboratory synthesis and industrial production.[104] As shown in Figure 20, a Cd^{2+}-based microporous metal-organic was synthesized by employing *meso*-tetra(N-methyl-4-pyridyl)porphine tetratosylate (TMPyP) as a template for the generation of porph@MOM-10 material.[48] Porph@MOM-10 showed promising applicability to undergo metal exchange affording efficient heterogeneous epoxidation catalysts. More specifically, the substitution of Cd^{2+} ions with Mn^{2+} and Cu^{2+} enhances the catalytic activity compared to the pristine porph@MOM-10. The porphyrin-based frameworks were used in the selective epoxidation of *trans*-stilbene as a typical reaction catalyzed by metalloporphyrins.

Table 1: Application of mixed-metal MOFs in heterogeneous catalysis

Entry	Catalyst	Mixed-Metal	Synthesis approach	Reaction	Take home message	Ref.
1	MIL-53	Al^{3+}/V^{3+}	Direct synthesis	Condensation of glycerol with acetone	Enhanced conversion compared to MIL-53(Al) (from 12.5% to 75.9% as the V^{3+} content increases)	105
2	MOF-74	Cu^{2+}/Co^{2+}	Direct synthesis	Styrene oxidation	Synergistic effect of Cu^{2+} and Co^{2+} in one framework (conv. 30.4%)	103
3	MIL-100	Sc^{3+}/Fe^{3+}	Direct synthesis	Alcohol oxidation, Tandem C-C Bond Formation	Higher catalytic activity of mixed-metal MIL-100 compared to MIL-100 (Sc) (yield > 48% *vs.* < 10%)	55
4	MOF-74	Ni^{2+}/Co^{2+}	Post-synthetic exchange in DMF	Oxidation of cyclohexene	Superior catalytic performance compared with pure Co-MOF-74 (conv. 61% *vs.* 4.7%)	102
5	$\{[CuM(pdc)_2(H_2O)_x]\cdot YH_2O\}_n$ (x= 0, 3, 4, 5, Y= 0-2)	Cu^{2+}/Mg^{2+} Cu^{2+}/Ca^{2+} Cu^{2+}/Sr^{2+} Cu^{2+}/Ba^{2+}	Direct synthesis	Epoxidation of olefins followed by epoxide ring opening	Enhanced activity with an increase in the size of the alkaline-earth metals ($TOF_{Cu/Mg}$ = 533 *vs.* $TOF_{Cu/Ba}$ = 103 for cyclohexene)	106
6	UiO-66	$Zr^{4+}/Ce^{3+,4+}$	Direct synthesis	Catalytic decomposition of methanol into CO_2	Enhanced binding of methanol in the substituted material	107
7	MIL-101	$Cr^{3+}/Ce^{3+/4+}$ (modified with Pd NPs)	Direct synthesis	H_2 production from ammonia borane	Synergistic effect between Pd NPs and Ce doped MOFs ($TON_{Pd/Ce\text{-}MIL}$ = 2357 *vs.* $TON_{Pd/MIL}$ = 977)	108
8	ZIF-8	Zn^{2+}/Cu^{2+}	Direct synthesis	Cycloaddition of organic azides with alkynes, Friedländer and	High stability and the ease of regeneration	109

				Combes condensations		
9	$[CoNi(\mu_3\text{-tp})_2(\mu_2\text{-pyz})_2]$	Co^{2+}/Ni^{2+}	Direct synthesis	Dye removal	Good activity and stability	[110]
10	MFM-300(Ga_2)	Ga^{3+}/Fe^{3+}	Direct synthesis	Epoxide ring-opening, acetylation of benzaldehyde	Higher conversion rates than MFM-300(Ga_2) for the ring-opening reaction (98% *vs.* 46% for styrene oxid)	[111]
11	$\{[Zn_2(L)(H_2O)_2]\cdot(5DMF)\cdot(4H_2O)\}$	Zn^{2+}/Cu^{2+}	Post-synthetic exchange in DMF	Knoevenagel condensation	Size-selective catalyst	[112]
12	porph@MOM-10	Cd^{2+}/Mn^{2+} Cd^{2+}/Cu^{2+}	Post-synthetic exchange in CH_3OH	Epoxidation of *trans*-stilbene	Metalloporphyrins as a template for the generation of MOFs	[48]
13	$[In_xGa_{1-x}(O_2C_2H_4)_{0.5}(hfipbb)]$	Ga^{3+}/In^{3+}	Direct synthesis	A^3 Strecker Reaction	Control of activity by modulating the ratio of metals	[113]
14	ZIF-8	Zn^{2+}/Ni^{2+}	Post-synthetic exchange in *n*-hexane	Electroreduction of CO_2	Excellent TOF (5273 h^{-1}) with a Faradaic efficiency for CO production of 71.9%	[114]
15	NH_2-UiO-66	Zr^{4+}/Ti^{4+}	Post-synthetic exchange in DMF	CO_2 reduction and hydrogen evolution	Facilitated electron transfer through Ti substituent	[81]
16	UiO-66	Zr^{4+}/Ti^{4+}	Post-synthetic exchange in DMF	CO_2 reduction to HCOOH	More efficient photocatalyst compared to NH_2-MIL-125(Ti) (TON ~ 6.27 *vs.* 1.52)	[115]
17	UiO-67	Zr^{4+}/Ti^{4+}	Post-synthetic exchange in DMF	Degradation of methylene blue	Improved photocatalytic reaction by the communication of the Ru with the Ti	[116]
18	UiO-66	Zr^{4+}/Ti^{4+}	Post-synthetic exchange through microwave-assisted reaction	PCVG to reduce Se^{6+}	Higher activity than either UiO-66 or a simple mixture of UiO-66 and $TiCp_2Cl_2$	[36]
19	NDC-MOFs	Zr^{4+}/Ti^{4+}	Post-synthetic exchange in DMF	Cascade MPV reduction and Etherification	Beneficial effect on the final activity (conv.$_{Zr/Ti\text{-}NDC}$ = 90% *vs.* conv.$_{Zr\text{-}NDC}$ = 19%, MPV of methoxybenzaldehyde)	[117]
20	MIL-101	Cr^{3+}/Fe^{3+}	Direct synthesis	Dye degradation	High photo-Fenton activity and stability	[118]
21	MMPF-5	Cd^{2+}/Co^{2+}	Post-synthetic exchange in DMSO	Epoxidation of *trans*-stilbene	Higher activity than the homogeneous (tdcmpp(Co)) catalyst (conv. 87% *vs.* 28.1%)	[119]

H_2Pdc = pyridine-2,5-dicarboxylic acid, tp = terephthalic acid, pyz = pyrazine, MFM-300(Ga_2); ($[Ga_2(OH)_2(L)]$), H_4L = biphenyl-3,3′,5,5′-tetracarboxylic acid), L = 2′-amino-[1,1′:3′,1′′-terphenyl]-3,3′′,5,5′′-tetracarboxylic acid ligand, porph@MOM-10= $Cd_6(BPT)_4Cl_4(H_2O)_4]\cdot[C_{44}H_{36}N_8CdCl]\cdot[H_3O]\cdot$[solvent], H_2hfipbb = 4,4′-(hexafluoroisopropylidene) bis(benzoic acid), PCVG= photochemical vapor generation, NDC = 2,6-naphthalendicarboxylate, MPV = Meerwein-Ponndorf-Verley, MMPF= metalmetalloporphyrin framework, tdcmpp= tetrakis(3,5-dicarboxymethylesterphenyl)porphine.

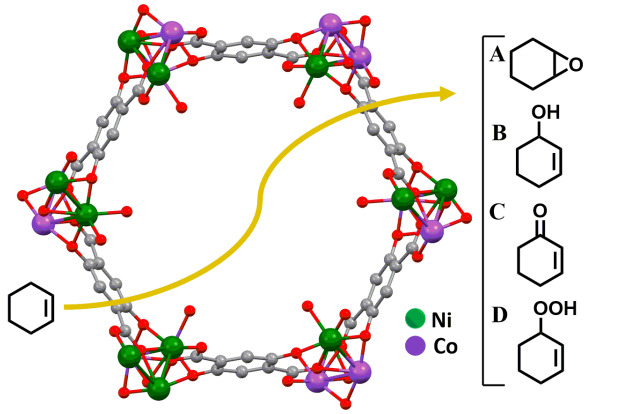

Figure 19: Aerobic oxidation of cyclohexene using Co/Ni-MOF-74. Reproduced from ref. [102] with permission. Copyright 2015, the American Chemical Society.

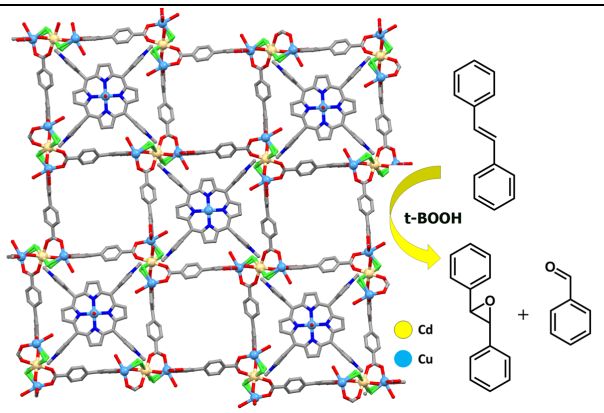

Figure 20: Post-synthetic metal exchange in porph@MOM-10 for styrene epoxidation. Reproduced from ref. [48] with permission. Copyright 2012, the American Chemical Society.

Similar to the blank reaction, porph@MOM-10 has a low activity in the epoxidation reaction showing a conversion < 10%. The improved activity is observed in the case of Mnporph@MOM-10-Mn and Cuporph@MOM-11-CdCu with 75% (turnover number (TON) = 178) and 79% (TON = 182) conversion of *trans*-stilbene respectively. The epoxidation reactions were performed in the presence of *tert*-butyl hydroperoxide (TBHP) as oxidant and stilbene oxide and benzaldehyde were the major products.

Another type of porphyrin-based MOF denoted as MMPF-5, is synthesized consisting of Cd^{2+}-metallated tetrakis(3,5-dicarboxyphenyl)porphine (tdcpp(Cd)) moieties that are connected to triangular $Cd(CO_2)_3$ moieties.[119] MMPF-5(Co) was obtained by placing crystals MMPF-5 into a DMSO solution of $Co(NO_3)_2$. The catalytic activity of the bimetallic porphyrin-based framework was evaluated in the epoxidation of *trans*-stilbene using TBHP as oxidant in acetonitrile at 60°C. The control experiments revealed the higher efficiency of MMPF-5(Co) exhibiting a great yield of 87% with 81.5% selectivity towards the epoxide product. The inactivity of MMPF-5 and low activity of the homogeneous tdcmpp(Co) catalyst (28.1% yield) highlights the importance of synthesized MM- porphyrin-based framework in the mentioned reaction. Furthermore, no significant leaching of the Co species was observed. So far, the activity of MM-MOFs has been examined only for styrene epoxidation and no studies were done to expand the substrate scope to other more challenging substrates such as linear olefins.

5.3. Condensation Reactions

MM-MOFs show promising applications in a variety of condensation reactions to generate useful cyclic organic compounds such as solketal and quinoline derivatives. Recently, Jhung *et al*. has nicely compared the influence of the metallic centers in a series of isostructural MOFs of the MIL family based on M^{3+} ions.[105] This study provides an insight into the correlation between the nature of the metal ions and catalytic performance for the synthesis of solketal from acetone and glycerol over catalytic MOF materials, namely, MIL-100(M) and MIL-53(M) (M = V, Al, Fe and Cr), as well as mixed MIL-53 (Al/V). The main products of the condensation reaction were a five-membered solketal (2,2-dimethyl-1,3-dioxane-4-methanol, (II)) and a six-membered acetal (2,2-dimethyl-dioxane-5-ol,(III)) as depicted in Figure 21. It was found that the glycerol conversion and isomer selectivity rely on different parameters including the nature of the metal ion, the length of the M-O bond, exchange of the coordinated water molecules and the presence of Brønsted acidity. Therefore, the highest conversion of glycerol is observed in the presence of MIL-100(V) (85.4%) and MIL-47(V) (75.9%) due to the higher acidity and easier replacement of water molecules by the reactants. A similar catalytic behavior of MIL-53(Al/V) samples with mixed metal-oxide clusters in the SBU was observed. The conversion of glycerol increases from 12.5 to 57.7%, as the vanadium content increases from 0 in MIL-53 (Al) to 75% in MIL-53 (Al/V)(25/75) with high selectivity (> 90%) towards the five-membered solketal (II).

Doping of ZIF-8 with Cu^{2+} ions through the direct reaction of $Cu(NO_3)_2$, $Zn(NO_3)_2$, and 2-methylimidazole under solvothermal conditions results in the formation of Cu/ZIF-8 material (Figure 22) with preserving the thermal stability (up to 350°C in air) and

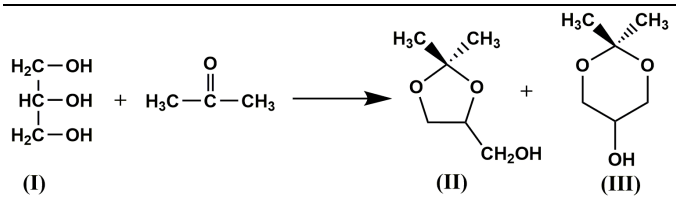

Figure 21: Condensation of glycerol with acetone over a series of MIL catalysts. Reproduced from ref. [105] with permission. Copyright 2017, Elsevier.

crystallinity of ZIF-8.[109] Molar percentages of 1, 5, 10 and 25% of $Cu(NO_3)_2$ to $Zn(NO_3)_2$ were applied to prepare bimetallic ZIF materials. Even at high dopant percentage of Cu^{2+} ions within the backbone (25% Cu relative to Zn) only a slight decrease of the specific area and pore size was observed ($Cu_{25\%}$/ZIF-8: ~ 1205 m^2g^{-1} and 0.44 cm^3g^{-1}, ZIF-8: 1700 m^2g^{-1}, 0.662 cm^3g^{-1}). However, at a higher doping percentage (50%) the framework decomposes. For catalysis, the Cu^{2+} doping significantly enhances the Lewis acidity of the ZIF-8 which is desirable for achieving high catalytic activity for Friedländer reaction of 2-aminobenzophenone with an active methylene compound catalyzed by the Cu/ZIF-8 material. Furthermore, the Combes condensation of aniline with acetylacetone under solvent-free conditions was studied. Using the Cu5%/ZIF-8 catalyst, the corresponding quinoline was isolated in 96% yield after 5 h at 100°C. The catalyst was reused for five consecutive runs without a decrease in the yield.

5.4. Tandem Reactions

Tandem or cascade reactions consist of two or more individual reactions combined in a single system without isolating and purifying the intermediates.[95] Therefore, this reaction is one of the ambitions in heterogeneous catalysis. Initially, the reactants are reacted by the first type of active site to generate an intermediate that is further catalyzed by the second type of active site to provide the desired product. As a critical note, truly interesting catalysts would be of the kind that outperform the simple mixture of two MOFs, in other words that form a transition state between the two metals and the substrate. Such reports, however, are very rare. One of the main features of MM-MOFs is the possibility to develop this kind of

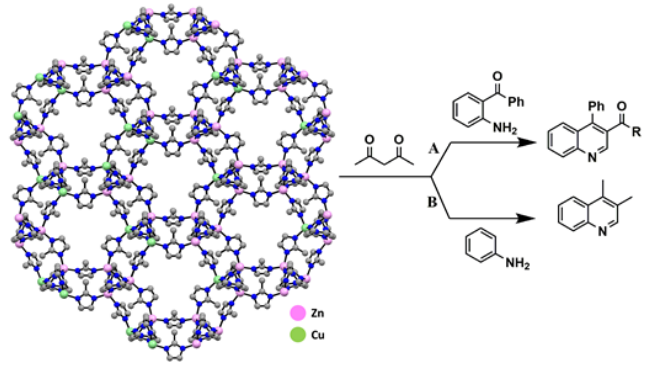

Figure 22: Cu-doped ZIF-8 for Friedländer and Combes condensations. Reproduced from ref. [109] with permission from the Royal Society of Chemistry.

with permission.multifunctional solid catalysts. An elegant example is the synthesis of MM-MOFs with the general formula $[In_xGa_{1-x}(O_2C_2H_4)_{0.5}(hfipbb)]$ ($H_2hfipbb$ = 4,4′ (hexafluoroisopropylidene) bis(benzoic acid)).[113] The obtained isostructural MOFs were applied in the three-component one-pot Strecker reaction between benzaldehyde, aniline, and trimethylsilyl cyanide (TMSCN) under solvent-free conditions (Figure 23). Both the monometallic (Al, Ga, In) and bimetallic (In, Ga) compounds were found to exhibit high activity in the mentioned reaction. The monometallic MOFs displayed distinctive behavior in this catalytic reaction producing three different products that are shown in Figure 23. More specifically, AlPF-1 resulted in 99% yield of the expected aminonitrile product (A) with a TON value of 99. In contrast, GaPF-1 gave the aldehyde cyanosilylation product (B) with 99% yield. It is mentioned that the quick activation of both the silyl and carbonyl groups followed by reaction with TMSCN inhibited the imine formation. On the other hand, the imine product (c) was formed over InPF-1. Interestingly, the combination of both metal ions, $In_{0.28}Ga_{0.72}$PF-3 MOF, could give the desired α-aminonitrile product within 0.33 h. The results confirm that the presence of a small amount of indium is sufficient to promote the imine formation over the aldehyde cyanosilylation. The presence of Lewis acid sites results in the benzaldehyde activation followed by the imine formation. Hereafter, the Lewis base-activated TMSCN attacked the imine group, giving α–aminonitrile. This study shows the possibility to tune the catalytic activity of MM-MOFs through modulating the ratio of active metal sites. In another example, a three dimensional M^{3+} trimesate catalyst MIL-100 (Sc/Fe) was synthesized, with Fe^{3+} as well as Sc^{3+} as framework sites.[55] The coordinately unsaturated metal sites can effectively be used in oxidation catalysis. The MIL-100 framework is a great potential host for the active sites due to its large surface area with accessible cages. The catalytic activity of this catalyst was tested for the Lewis acid-catalyzed tandem Friedel–Crafts addition reaction between 2-methylindole and trifluoroacetaldehyde ethyl hemiacetal followed by oxidation of the product in the presence of TBHP (Figure 24). The first two steps of the reaction (deacetalization and alkylation) proceed through Sc^{3+} Lewis acid sites, while the Fe^{3+} sites promote alcohol oxidation. More interestingly, this study showed that tandem reactions may overcome the usual diffusion limitations of reactants since *in situ* generated intermediates are located near the active sites. Therefore, enhanced catalytic performance can be observed compared to an individual process.

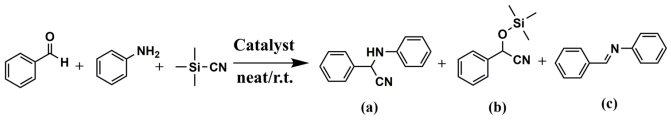

Figure 23: One-pot Strecker reaction using benzaldehyde, aniline, and TMSCN. Reproduced from ref. [113] with permission. Copyright 2015, the American Chemical Society.

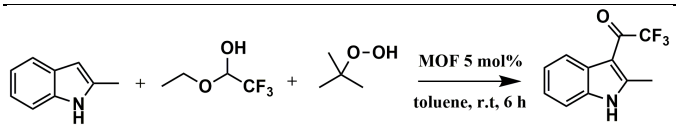

Figure 24: Tandem Friedel–Crafts addition and oxidation reaction catalyzed by MIL-100 (Sc/Fe). Reproduced from ref. [55] with permission. Copyright 2014, John Wiley & Sons, Inc.

In another tandem reaction, a bimetallic NDC-MOF (Zr/Ti) (NDC = 2,6-naphthalene-di-carboxylate) was developed and used as catalyst for the Meerwein-Ponndorf-Verley (MPV) reduction etherification of *p*-methoxybenzaldehyde with butanol (Figure 25).[117] The process involves the reduction of 4-methoxybenzaldehyde to the corresponding alcohol followed by the etherification. The NDC-MOF (Zr/Ti) having more than one type of Lewis acid site in the framework demonstrates higher activity and selectivity than the parent Zr-NDC material.

5.5. CO_2 Reduction Reaction (CRR)

Besides the capture and storage of CO_2, another appealing strategy is the conversion of CO_2 into fuels or chemical stocks, which is an ideal way to alleviate the environmental problems as this will not only reduce the atmospheric CO_2 levels but also decrease the fossil fuel consumption. Nevertheless, due to the chemical inertness of the CO_2 molecule, appropriate catalysts are required to convert large quantities of CO_2 into the production of valuable chemicals such as carbon monoxide (CO), formic acid (HCOOH) and formaldehyde (HCHO). MM-MOFs, which have already shown their capability in a variety of applications, have the potential to selectively reduce CO_2. Recently, a single-atom catalyst having Ni sites was synthesized with the aid of a MOF for efficient electroreduction of CO_2 [114]. The synthesis was based on the ionic exchange between Zn nodes of pristine ZIF-8 with Ni^{2+} ions followed by pyrolysis at 1000°C. This synthesis process gave a nitrogen doped porous carbon material with well dispersed single Ni sites providing improved electronic conductivity. The resultant material demonstrated a great turnover frequency (5273 h^{-1}) for CRR with a high Faradaic efficiency (FE) of 71.9% for CO evolution at an overpotential of 0.89 V. Cohen *et al.*[115] investigated the photocatalytic reduction of CO_2 to HCOOH over a mixed-ligand, MM-MOF under visible light irradiation. It has been proved that the presence of a small amount of 2,5-diaminobenzene-1,4-dicarboxylic acid ($(NH_2)_2$-BDC) as a co-ligand followed by Ti substitution significantly boosts the photocatalytic activity compared to original UiO-66(Zr)-NH_2 framework. The TON values of UiO-66(Zr/Ti)-NH_2 (4.66 ± 0.17) with only NH_2-BDC linkers is lower than the 1(Zr/Ti) (6.27 ± 0.23) having NH_2-BDC and ($(NH_2)_2$-BDC) linkers. The presence of diamine-substituted linkers considerably enhances the photocatalytic activity by introducing new energy levels for additional light absorption and charge transfer. Additionally, the improved catalytic activity compared to monometallic UiO-66(Zr) was associated with the lowered redox potential energy level of the bimetallic material resulted from the partial replacement of Ti ions with Zr ions in the $Zr_6O_4(OH)_4$ SBUs.

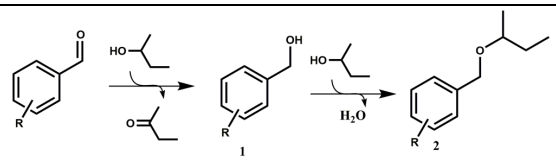

Figure 25: MPV reduction of the aldehyde to alcohol with successive etherification catalyzed by NDC-MOF (Zr/Ti). Reproduced from ref. [117] with permission from the Royal Society of Chemistry.

5.6. Photocatalysis

An interesting class of materials for photocatalysis is the class of Ti-based MOFs because of their photocatalytic features, redox activity and the low toxicity of Ti. MIL-125 was the first Ti-based MOF that exhibited photocatalytic activity under UV radiation.[120] Nevertheless, the synthesis of Ti-based MOFs is still challenging and few relevant Ti-based MOFs have been reported.

The post-synthetic exchange process is another alternative to obtain heterometallic MOFs with Ti as the desired active sites for photocatalysis. A multifunctional UiO-67-based MOF has been synthesized using the prefunctionalized Ru(bpy)$_2$(5,5'-dcbpy) linker followed by post-synthetic metal exchange process to include Ti sites (Figure 26).[116] The prepared MOF was applied for photocatalytic degradation of methylene blue (MB) in aqueous solution under visible irradiation (419 nm). These results confirm that the photocatalytic reaction is promoted through the synergistic effect between the Ru complex to work as a light antenna and Ti as photocatalyst. Still, the photocatalytic activities of most (all) MOFs are not yet competitive to the robust and cheap titania materials. After the first synthesis of a Ti-doped Zr-UiO-66 by Cohen *et al.*[35], we have shown recently the enormous impact on the bandgap of doping the Zr-UiO-66 with Ti^{4+}, Ce^{4+}, and different lanthanides on the photochemical behavior of these MOFs. We were able to synthesize following doped and pure MOFs, using the microwave synthesis procedure[121]. The UiO-66(Ce) also exists as a pure monometallic MOF. Combination of modelling and experimental results showed how doping could enhance the photocatalytic activities of these MOFs, by drastically changing the band gap of these materials. This is shown in Figure 27 with a concluding diagram.

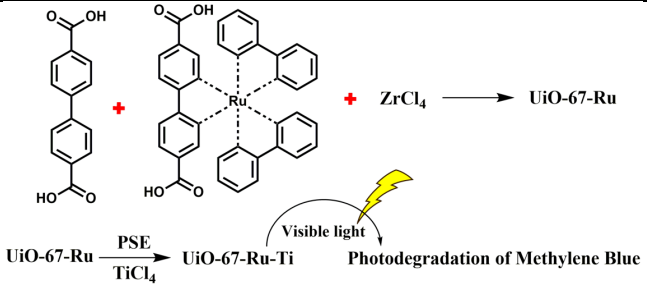

Figure 26: Synthesis procedure of UiO-67(Ru/Ti) for photodegradation under visible light. Reproduced from ref.[116] with permission from the Royal Society of Chemistry.

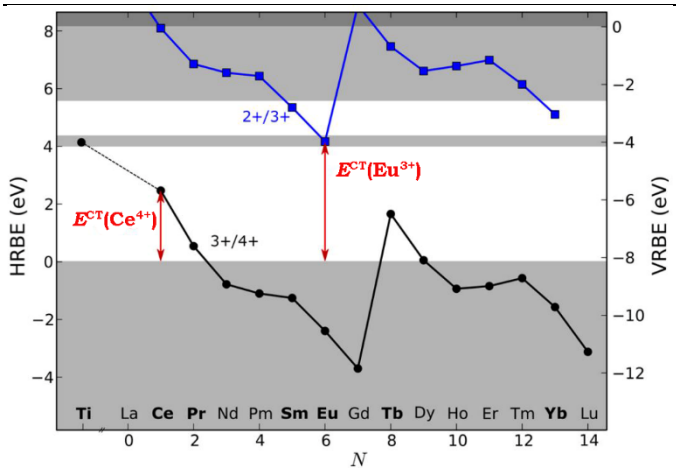

Figure 27: Overlay of the band diagram of UiO-66 (gray) with both the (3+/4+) (black dots) and (2+/3+) charge state transition levels (blue squares) for the lanthanide series incorporated as impurities in the UiO-66 host. Elements with a potentially interesting transition level for photocatalysis are printed in bold. The curves are calibrated using the CT absorption edges obtained for UiO-66:Ce^{4+} (3+/4+) and UiO-66:Eu^{3+} (2+/3+) as indicated by the red arrows. Values are referred to the vacuum (VRBE, vacuum-referred binding energy) or relative to the host material (HRBE, host-referred binding energy). Reprinted from reference[121] with permission. Copyright 2018, the American Chemical Society.

From the diagram in Figure 27, it is observed that the $Ti^{(3+/4+)}$ level and hence the CT of Ti^{4+} is resonant with the material's HOMO–LUMO gap, explaining the improved electron mobility of UiO-66/5%Ti^{4+} after excitation. The overlap between the $Ti^{(3+/4+)}$ level and the LUMO of UiO-66 is believed to be the cause for the increased photocatalytic activity for UiO-66/5%Ti^{4+}, since an excited electron of the linker has sufficient energy to move to the dopant ion. Following the same reasoning, all Ln ions with (3+/4+) or (2+/3+) charge state transition levels near or below the UiO-66 LUMO region could potentially be the target of an LMCT process upon excitation of the UiO host (e.g., Pr, Sm, or Tb). While revising the review, Gagliardi and Truhlar published similar results, this time on the doping of the UiO-66(Ce) with Ti^{4+} and Zr^{4+}[122]. They concluded that the Titanium doped Ce-UiO-66-I (iodine functionalized BDC linkers) shows potential for the unbiased water-splitting reaction.

5.7. Challenges in Catalysis

A major challenge in preparing these types of bimetallic catalysts remains the control and optimization of the ratio of the active components. It has been proved that the catalytic properties can be tuned by varying the ratio of the active sites. In some cases, an increase in the ratio of one of the active sites results in a higher catalytic activity but an absolute reduction in A major challenge in preparing these types of bimetallic catalysts remains the control and optimization of the ratio of the active components. It has been proved that the catalytic properties can be tuned by varying the ratio of the active sites. In some cases, an increase in the ratio of one of the active sites results in a higher catalytic activity but an absolute reduction in the selectivity towards the desired product. On the other hand, the reaction environment and the applied conditions play a key role in catalytic performance. Hence, the control of activity and selectivity may be complicated in some of these bimetallic systems. Another main obstacle in the development of bimetallic catalysts with controlled activity and selectivity is due to the limited knowledge of the precise mechanism over these catalysts. Despite many researchers proved the synergistic effect of active sites to be responsible for the enhanced catalytic activities, particular attention should be paid to the real nature of active sites and the reaction mechanisms. The combination of control experiments and computational approaches may offer good opportunities to elucidate these issues. Additionally, the use of Mixed-metal MOFs in heterogeneous catalysis is mainly restricted to some simple liquid-phase reactions. Definitely, there is a requirement to expand their applications to other reaction systems such as multicomponent reactions to develop new directions for the applications of these promising catalysts.

6. Mixed-Metal MOFs in Gas Adsorption and Separation

The tuning of MOFs by the mixed-metal approach has huge implications on their flexibility that might be one of the important factors to create tailor made adsorbents for selective gas storage and release. In this section, selected examples of MM-MOFs for gas adsorption and separation are described. A summary is shown in Table 2.

6.1. CO_2 adsorption

By using the mixed-metal strategy a family of isostructural heterometallic MOFs (CPM-200 series) with combinations of trivalent (In^{3+}, Ga^{3+}, Fe^{3+}, V^{3+}, Sc^{3+}) and divalent metals (Mg^{2+}, Mn^{2+}, Co^{2+}, Ni^{2+}) has been reported by Feng *et al.* (Figure 28).[123] This M^{2+}/M^{3+} heterometallic combination allows for a strong tuning of the CO_2 adsorption and the CO_2 /N_2 selectivity. A high CO_2 uptake was obtained with the Mg^{2+} CMP-200 series, in the order of Fe^{3+}/Mg^{2+} > In^{3+}/Mg^{2+} > V^{3+}/Mg^{2+} > Ga^{3+}/Mg^{2+} > Sc^{3+}/Mg^{2+}. The CMP-200 (Fe^{3+}/Mg^{2+}) showed the highest CO_2 adsorption, being 9.27 mmol/g at 273 K and 1 bar. Furthermore, the CMP-200 (V^{3+}/Mg^{2+}) has an isosteric heat of adsorption for CO_2 of -79.6 kJ/mol which is the highest of all reported MOFs. A correlation between charge-to-radius ratio (z/r) of metal cations and isosteric heat for CO_2 in the mixed-metal combinations was suggested as the driving force for the selectivity. In another investigation, Orcajo *et al.*[124] found that after partial exchange of Zn^{2+} ions with Co^{2+} ions in MOF-5, the CO_2 adsorption capacity is higher than in the pure (Co^{2+}-free) analogue. The authors used a one-pot procedure to incorporate different amounts of Co^{2+} ions (8% and 21%) into Zn-MOF-5. The substitution

of Co^{2+} ions in the Zn_4O cluster was limited and could not exceed 25%. A color change from pink to blue was observed upon the removal of two coordinated DEF molecules per Co ion in Co-doped MOF-5, due to changes in the geometry of Co^{2+} ions from octahedral to tetrahedral. The CO_2 adsorption increased proportionally with the content of Co^{2+}.

Table 2: Application of mixed-metal MOFs in gas adsorption.

Entry	adsorbent	Mixed-Metal	application	Synthesis approach	Take home message	Ref.
1	CPM-200	Sc^{3+}/Mg^{2+}, Mg^{2+}/Ga^{3+}, Mg^{2+}/Fe^{3+}, Mg^{2+}/V^{3+}	CO_2, H_2 Adsorption	Direct synthesis	Superior CO_2 uptake capacity: up to 207.6 cm^3/g at 273 K and 1 bar	[123]
2	MOF-5	Zn^{2+}/Co^{2+}	H_2, CH_4, CO_2 Adsorption	Direct synthesis	Co^{2+} is incorporated into unexposed metal sites that are less accessible to gas molecules	[124]
3	MIL-101	Cr^{3+}/Mg^{2+}	CO_2 Adsorption, CO_2/N_2 selectivity	Direct synthesis	Increased CO_2 adsorption up to 40% compared to MIL-101(Cr): 3.28 mmol/g at 298 K and 1 bar	[125]
4	MOF-74	Zn^{2+}/Co^{2+}	H_2, CH_4, CO_2 Uptakes	Direct synthesis	Enhanced H_2, CH_4 and CO_2 (53.72% *vs.* 46.96% at 0 °C and 10 bar) uptake with increasing Co^{2+} content	[126]
5	MOF-74	Co^{2+}/Ni^{2+}	H_2 Adsorbent	Direct synthesis	Higher H_2 adsorption capacity with 40% Ni^{2+} content due to the smaller pore size	[127]
6	COMOC-2	Al^{3+}/V^{4+}	CO_2 Adsorption	Direct synthesis	Novel, large pore phase in the bimetallic Al^{3+}/V^{4+} MOF	[57]
7	Mg-MOF-74	Mg^{2+}/Co^{2+} or Ni^{2+}	CO_2 Adsorption	Direct synthesis	High water stability while maintaining high CO_2 uptake capacity	[28]
8	HKUST-1	Cu^{2+}/Zn^{2+}	HD Adsorption and desorption	Direct synthesis	Detailed study on the adsorption of small molecules by Three-pulse ESEEM spectroscopy	[69]
9	Mg-MOF-74	Cd^{2+}/Mg^{2+}	CO_2 Adsorption	Direct synthesis	Weaker binding energies for CO_2 adsorption with the incorporation of Cd^{2+}	[94]
10	MIL-53	Cr^{3+}/Fe^{3+}	CO_2 Adsorption	Direct synthesis	Tuning the breathing behaviour by cation mixing	[26]
11	MIL-53	Cr^{3+}/V^{3+}	CO_2 Adsorption	Direct synthesis	Microwave induced ''egg yolk'' structure in MIL-53 (Cr^{3+}/V^{3+})	[27]
12	CTOF-1 CTOF-2	Co^{2+}/Ti^{4+}	H_2, CH_4, CO_2 Adsorption	Direct synthesis	Permanent porosity and irreversible phase transition between two stable forms	[128]
13	UiO-66	Zr^{4+}/Ti^{4+}	CO_2 Adsorption	Post-synthetic exchange in DMF	Superior CO_2 uptake, 4 mmol g^{-1} *vs.* 2.2 mmol g^{-1} at 273 K and 1 bar	[82]
14	Ni-ITHD	Ni^{2+}/Zn^{2+} Ni^{2+}/Co^{2+}	CO_2 Uptake	Direct synthesis,	Ultra large CO_2 uptake capacity (2.71 g g^{-1}) at 1 bar and 195 K	[129]

				post-synthetic exchange in DMF		
15	PCN-922	Zn^{2+}/Cu^{2+}	H_2, CH_4, CO_2 Adsorption	Post-synthetic exchange in DMF	Higher porosity and gas adsorption capacity compared to PCN-922(Zn), 142.97 cm^3g^{-1} at 273	130
16	CPM-18 CPM-19 CPM-20 CPM-21 CPM-23	In^{3+}/Nd^{3+}, Sm^{3+}, Pr^{3+}, Mn^{2+}, Co^{2+}, Cu^{2+}, Mg^{2+}	H_2, CO_2 Adsorption	Direct synthesis	Enhanced gas uptake capacity in the substituted material	131
17	$Mn_3[(Mn_4Cl)_3(BTT)_8(CH_3OH)_{10}]_2$	Mn^{2+}/ Li^+, Cu^+, Fe^{2+}, Co^{2+}, Ni^{2+}, Cu^{2+}, Zn^{2+}	H_2 Storage	Post-synthetic exchange in methanol	High H_2 storage capacity, ranging from 2.00 to 2.29 wt% at 77 K and 900 torr	132
18	CMP-15	In^{3+}/Co^{2+}, Mg^{2+}, Mn^{2+}, Ni^{2+}, Cd^{2+}	H_2, CO_2 Adsorption	Direct synthesis	New class of zeolite-type porous materials	131
19	ZIF-8	Co^{2+}/Zn^{2+}	CO_2, H_2 Uptakes	Direct synthesis	Enhancement of 30% in the CO_2 (0.9 mmol g^{-1} at 298 K and 1 bar) and 23% in the H_2 (7.69 mmol g^{-1} at 77 K and 1 bar) uptake	133
20	$Cd_3[(Cd_4Cl)_3(BTT)_8]_2$	Cd^{2+}/Co^{2+} Cd^{2+}/Ni^{2+}	H_2 Adsorption	Post-synthetic exchange in methanol	Good H_2 storage capacities for the mixed-metal material	134
21	MIL-53	Al^{3+}/Cr^{3+}	CO_2 Adsorption	Direct synthesis	Tuning the breathing effect	64
22	ZTOF-1	Zn^{2+}/Ti^{4+}	CO_2, H_2 Adsorption	Direct synthesis	Permanent porosity and long-term stability	135
23	UiO-66	Zr^{4+}/Ti^{4+}	CO_2 Separation	Post-synthetic exchange in DMF	CO_2 permeability enhancement of 153% at 298 K and 1 atm	136
24	iso1	Mn^{2+}/Cu^{2+}	CO_2 /CH_4 Separation, CH_3OH/ CH_3CN and CH_3CH_2OH vapor separation	Direct synthesis	High selectivity in the separation of small molecules	137
25	HKUST-1	Cu^{2+}/Li^+, Na^+, K^+	CO_2 Adsorption	Direct synthesis	Enhanced adsorption capacity, 8.64 mmol g^{-1} *vs.* 7.72 mmol g^{-1} at 298 K and 18 bar	138
CPM= crystalline porous material, COMOC= Center for Ordered Materials Organosilica and Catalysis, CTOF = cobalt-titanium organic framework, DMF= dimethylformamide, ITHD = ith-d net topology, PCN = porous coordination network, BTT= 1,3,5-benzenetristetrazolate, ZTOF = zinc-titanium-organic framework, iso = isoreticular						

The higher CO_2 capacity of the Co-doped MOF-5 was ascribed to the incorporation of Co^{2+} ions into unexposed metal sites that are less accessible to gas molecules. In another study, Ti-exchanged UiO-66 MM-MOFs were examined for their ability to improve the CO_2 uptake capacities.[82] Interestingly, the CO_2 adsorption capacity of UiO-66 at 273 K increased from 2.3 mmol g^{-1} to 4 mmol g^{-1} after partial replacement of Zr^{4+} by Ti^{4+} (representing an enhancement up to 81 wt.%). The exchanged UiO-66 (Ti/Zr) exhibits smaller pore sizes in comparison to the original UiO-66, and the interaction of CO_2 with Ti^{4+}-nodes is much stronger. Both phenomena contribute to the increase in CO_2 affinity. A similar Ti-UiO-66 system was studied as a mixed matrix membrane for the separation of CO_2 from N_2.[136] The resulting mixed Ti-UiO-66 membranes demonstrated an exceptional

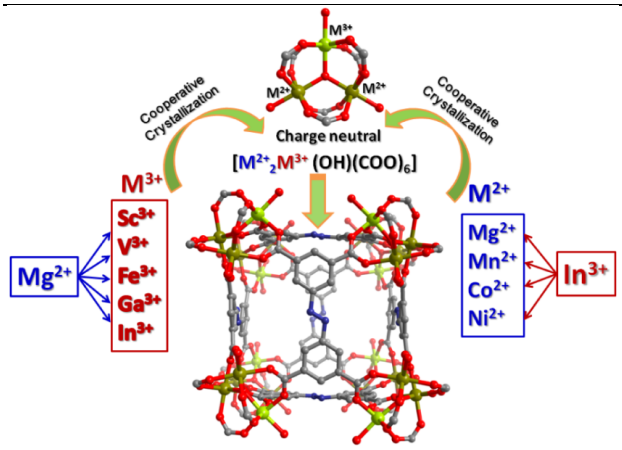

Figure 28: Structure of CMP-200-M^{2+}/M^{3+} series. Reprinted from ref. [123] with permission. Copyright 2016, the American Chemical Society.

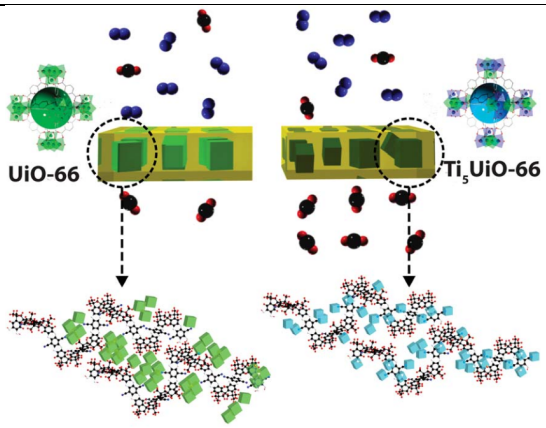

Figure 29: The CO_2 permeability of Ti-exchanged UiO-66 in comparison to a UiO-66. Reprinted from ref. [136] with permission. Copyright 2015, Springer Natur.

CO_2 permeability enhancement up to 153% when compared to the parent UiO-66 matrix membranes (Figure 29). This is again due to a combination of several factors. Next to the above mentioned stronger interaction of CO_2 with Ti^{4+}-nodes, the Ti^{4+} exchanged UiO-66 has a much better interaction with the membrane polymer (PIM-1), and was thus much better dispersed, as visualized in Figure 29.The partial substitution of Co^{2+} or Ni^{2+} into Mg^{2+}-MOF-74 resulted in an increased water stability while maintaining the high CO_2 uptake capacity.[28] The original Mg-MOF-74 has been reported to have the highest CO_2 adsorption capacity at 0.1 atm of all reported MOFs when dry CO_2 is used.[139-143] However, in humid conditions, the stability and recyclability are problematic, and water competes with CO_2 to bind on the active sites, resulting in a strongly reduced CO_2 uptake. On the other hand, other MOF-74 analogues with different metal nodes are reported to have a better stability in humid conditions but lower CO_2 adsorption capacities are recorded. In this regard, Walton *et al.*[28] improved the water stability of Mg-MOF-74 after incorporating 16 mol% Ni^{2+} in the framework. The lower stability of Mg-MOF-74 is related to the standard reduction potential of the metal ions. The lower stability of the Mg-MOF-74 is related to the relative instability of the Mg-O bonds and its high affinity to water. In the same water vapor pressure condition, the parent Mg-MOF-74 structure showed only 8% of surface area retention whereas 82% of the surface area is retained in the MOF-74 (Ni/Mg) compound. This is of course still not a competitive value.

Some MOFs can expand and contract reversibly, and are referred to as "breathing" MOFs. The breathing MOFs can undergo a drastic transformation in unit cell volume under an external stimulus such as temperature, pressure and guest molecules. Large porosity and great selectivity are two significant factors for the gas adsorption and separation. Serre *et al.*[26] reported the influence of mixing Cr^{3+} and Fe^{3+} cations on the breathing behavior of MIL-53. They noticed that the MM-MOF with a composition of Cr: 60%, Fe: 40% exhibits a breathing behavior that is totally different than that of MIL-53(Cr) and MIL-53(Fe). According to the PXRD, the hydrated *np* (narrow pore) form of the mixed-metal MIL-53(Cr/Fe) compound at 293 K changes to a *cp* (closed pore) form at 343K and it shows a *lp* (large pore) form upon further heating above 463 K (Figure 30). This breathing profile is different from both the monometallic compounds. MIL-53(Cr) shows a direct *np* to *lp* transformation and MIL-53(Fe) presents a two-step *np* to *cp* transformation. The bimetallic compound shows also a distinctly different CO_2 uptake isotherm with the *np* to *lp* transition at around 10 bar (that is intermediate between 3 bar for MIL-53(Cr) and more than 20 bar for MIL-53(Fe)) (Figure 30). So metal mixing in MOFs might be a promising approach to rationally fine tune the sorption behavior. We made a similar study in the isoreticular series of DUT-5 (an Al-biphenyldicarboxylate MOF) and COMOC-2 (the V-variant).[57, 144] (Figure 31). A combination of EPR, XANES, EXAFS and *in situ* XRD during CO_2 sorption revealed that the MM-MOFs, containing both V and Al, had in fact two *lp* forms, one that is flexible and exists in vacuum and undergoes reversible transformations to the *np* form, and one *lp* form that comes exclusively from the *np* form.

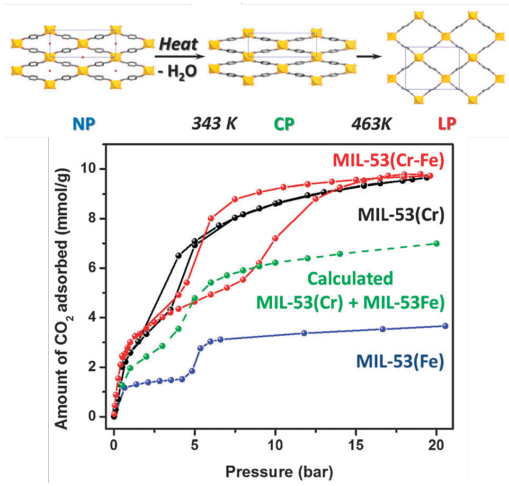

Figure 30: The phase transformation upon heating (top) and CO_2 adsorption isotherms at 283 K for the MIL-53 materials. Reproduced from ref. [26] with permission from the Royal Society of Chemistry.

6.2. H_2 adsorption

Also this study showed that the transition pressures are controlled by the metal mixing concentrations. Hydrogen storage is and remains one of the main applications of MOFs. Efforts to improve the hydrogen uptake have been done by tuning the pore size, insertions of metal nanoparticles, in creating extra unsaturated metal sites and by linker modification. But also MM-MOFs have been investigated for hydrogen storage. Long *et al*.[132] created a series of the mixed-cation version of the $Mn_3[(Mn_4Cl)_3(BTT)_8(CH_3OH)_{10}]_2$ for H_2 adsorption.[132] For a systematic tuning of the H_2 adsorption affinity, the cationic guest Mn^{2+} is partially substituted with Li^+, Cu^+, Fe^{2+}, Co^{2+}, Ni^{2+}, Cu^{2+}, and Zn^{2+} ions. All the materials showed relatively high H_2 uptakes ranging from 2.00 to 2.29 wt% at 77 K and 900 torr. Powder neutron diffraction experiments revealed that the coordination of H_2 to unsaturated Mn^{2+} sites is the reason for the high heat of adsorption of Mn^{2+} (10.1 kJ/mol). The mixed Co^{2+}/Mn^{2+} compound exhibited a higher enthalpy of adsorption about 10.5 kJ/mol in comparison to the monometallic version. A different approach was undertaken by Singh and coworkers.[133]

They synthesized a mixed metal ZIF-8 (Co^{2+}/Zn^{2+}) by partially exchanging Zn^{2+} by Co^{2+}. This MM-MOF showed an increase of pore volume compared to monometallic Zn^{2+}-ZIF-8. A remarkable enhancement of around 30% in the CO_2 and 23% in the H_2 uptake was demonstrated by the ZIF-8 (Co/Zn) (75% Co-containing) frameworks as compared to Zn-ZIF-8 under similar conditions. Again, the increase in pore volume and the affinity of the Co^{2+} are responsible for the higher hydrogen uptake.

7. Luminescence properties

Mixed-lanthanide MOFs form and intriguing class of MM-MOFs whose properties are not comparable to their homometallic counterparts. Such new mixed-lanthanide MOFs offer a wide range of applications such as luminescent thermometers[145-150], white-light emitting compounds[151], optical sensors[152, 153] and barcoded luminescent materials[154]. We published very recently a review on the use of luminescent MOFs for sensing applications.[155] Chen *et al*.[145] tuned the luminescent properties of MOFs, by creating a series of mixed-metal (Tb^{3+}, Eu^{3+}) MOFs. They doped a source of Eu^{3+} into $a[Tb_2(dmbdc)_3]_n$ (2,5-dimethoxy-1,4-benzenedicarboxylate) framework to form mixed-lanthanide MOFs. The resulting materials exhibit temperature-dependent luminescence. The dmbdc linker has a suitable triplet excited state energy to function efficiently as a sensitizer for Tb^{3+} and Eu^{3+} leading to green and red emission. In a series of mixed Eu_xTb_{1-x}-dmbdc MOFs, by increasing the temperature from 10K to 300 K, the emission intensities of the Tb^{3+} gradually decreased, while the Eu^{3+} luminescence increased due to the Tb^{3+} to Eu^{3+} energy transfer.

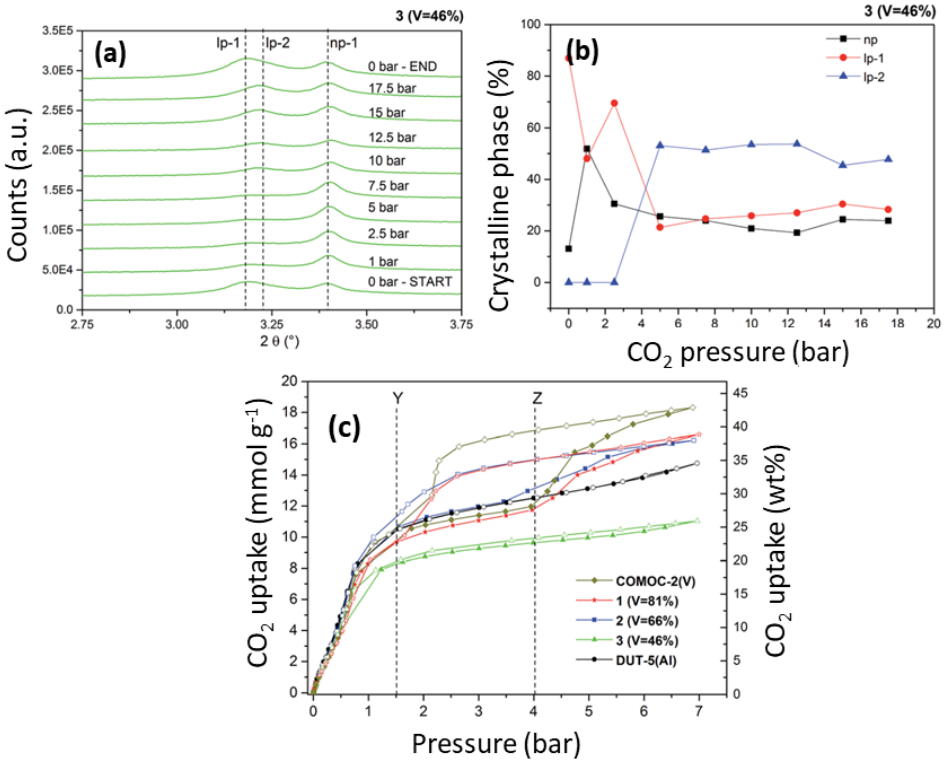

Figure 31: (a) High pressure CO_2 PXRD analysis of mixed-metal COMOC-2(Al/V) between 0 – 18 bar of CO_2 pressure at 233 K and (b) the corresponding Rietveld analysis; (c) High pressure CO_2 sorption measurements of COMOC-2(V), 1(V = 81%), 2 (V = 66%), 3 (V = 46%) and DUT-5(Al) from 0 to 7 bar at 228 K. Reproduced from ref. [57] with permission from the PCCP Owner Societies.

The luminescent $Eu_{0.0069}Tb_{0.9931}$-dmbdc compound displayed systematically temperature-dependent luminescence colors tuning from green-yellow to red upon heating from 10 to 300 K (Figure 32). The energy transfer among the lanthanide ions has enabled this very promising luminescent mixed-lanthanide MOF approach to realize practically valuable luminescent thermometers. Furthermore, they incorporated a new organic ligand with a higher triplet state energy, (H_2pia =5-(pyridin-4-yl)isophthalic acid), into the mixed-metal MOF. The new luminescent $Tb_{0.9}Eu_{0.1}$PIA thermometers demonstrated much higher relative sensitivity of 3.53% K^{-1} which is even higher than all other kinds of luminescent thermometers. By having a higher energy gap between the ligand and Tb^{3+}, the competitive energy back-transfer from Tb^{3+} to the ligand can restrict and therefore, more efficient energy transfer from Tb^{3+} to Eu^{3+} can occur in the bimetallic system at the elevated temperature[146]. The scale down of MM-MOF thermometers may increase their potential applications in many fields such as measuring the physiological temperatures in biological applications. In this regards, a luminescent nanothermometer was developed by Carlos *et al*.[147] The nanorods of TbEu-MOF were prepared by a reverse microemulsion method (average length and diameter of 300 and 30 nm, respectively). The $Tb_{0.99}Eu_{0.01}(BDC)_{1.5}(H_2O)_2$ MM-MOF was used as a temperature sensor in the physiological range (300–320 K), with high sensitivities in both water media and as solid probe. Aqueous suspensions of TbEu-MOF nanoparticles exhibit the emission quantum yield of 0.23±0.02 (excitation at 320 nm) and relative sensitivity of 0.37% K^{-1} at 318 K. Another interesting feature of the mixed-lanthanide MOFs is their near-infrared emissions (NIR) which can be applied in biological systems due to their small absorption or scattering. In this context, Qian *et al.*[148] designed a temperature sensitive NdYb-MOF for temperature sensing in the range of 293 K to 313 K under laser pumping. The monometallic YbBDC-F_4 (BDC-F4=2,3,5,6 tetrafluoro1,4-benzenedicarboxyla) was unable to produce any emission upon laser pumping at 808 nm while, the mixed $Nd_{0.577}Yb_{0.423}$BDC-F_4 MOF displayed the characteristic emissions of both Nd^{3+} and Yb^{3+} ions. This is implying the efficient energy transfer from Nd^{3+} to Yb^{3+} ions in the bimetallic MOF. The energy transfer from Nd^{3+} to Yb^{3+} ions enhanced by the increase in temperature at the physiological range (293–313 K) and showed a relative photoluminescence sensitivity of 0.816% K1 at 313 K.

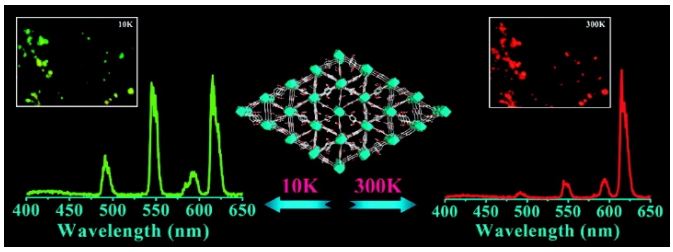

Figure 32: View of the structure and photographs of the luminescence, and emission spectra of the $Eu_{0.0069}$ $Tb_{0.9931}$-dmbdc MOF at 10 and 300 K upon excitation at 312 nm. Reprinted from ref. [145] with permission. Copyright 2012, the American Chemical Society.

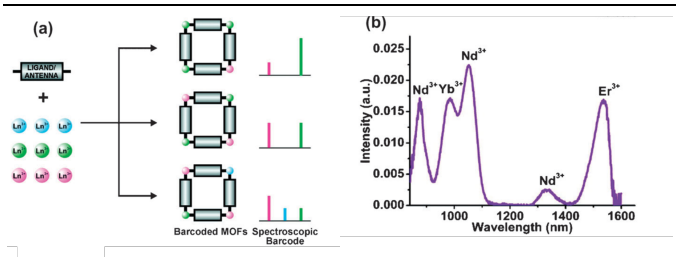

Figure 33: (a) Schematic representation of the approach to design photoluminescent barcoded systems based on the use of multiple NIR-emitting Ln^{3+} ions. (b) Nd^{3+}, Yb^{3+} and Er^{3+} emission from $Nd_{0.09}Er_{0.55}Yb_{0.36}$-PVDC MOF. Reprinted from ref. [154] with permission. Copyright 2009, the American Chemical Society.

Luminescent MOFs can be designed as turn-off or turn-on sensors for organic molecules, especially nitroaromatic explosives. Recently, Huang *et al*.[151] reported the use of a $Tb_{0.01}Gd_{0.99}$L mixed-metal MOF (H_4L=[1,1′:4′,1″-terphenyl]-2′,4,4″,5′-tetracarboxylic acid) for the sensing of picric acid. Upon the addition of picric acid (from 0 to 100 μM) into the Tris−HCl buffer suspensions of $Tb_{0.01}Gd_{0.99}$L as a dual emission mixed- Lanthanide compound, the Tb^{3+} emission decreases slowly; however, the ligand-based emission was sharply quenched. The linear relationship of $I(^5D_4 \rightarrow {}^7F_5)/I(L)$ intensity ratio and concentration of picric acid shows that the $Tb_{0.01}Gd_{0.99}$L is a good ratiometric luminescence sensor material for picric acid. Another feasible application of the mixed-lanthanide MOFs has been reported by Petoud *et al*. as luminescent-barcoded materials (Figure 33).[154] The new barcode system operation is based on mixed-lanthanide MOFs that simultaneously emit several independent NIR signals. These mixed-lanthanide-MOFs display sharp NIR-emission signals from both Yb^{3+} (980 nm) and Er^{3+} (1530 nm) (excitation at 490 nm). In this regard, a series of Er_xYb_{1-x}-PVDC MOFs (x= 0.32, 0.58, 0.70, and 0.81) were designed (H_2PVDC = 4,4′-[(2,5- dimethoxy-1,4-phenylene)-di-2,1-ethenediyl]bisbenzoic acid). The emission intensity of Er^{3+} and Yb^{3+} varies linearly with their concentration. The respective emission intensities of the lanthanide ions can be quantitatively altered by controlling the lanthanide composition in order to obtain unique NIR barcode fingerprints (Figure 33).

Also, more complicated barcode signal can be obtained by incorporating additional lanthanide ions in the same framework. This approach can increase the number and diversity of barcodes as demonstrated by $Nd_{0.09}Er_{0.55}Yb_{0.36}$-PVDC MOF consisting of concurrent NIR emissions from all three lanthanide ions.

8. Conclusion and outlook

Mixed-metal MOFs are still in their infancy. Using combinations of advanced spectroscopic techniques, several materials have now been proven without any doubt to be true MM-MOFs, i.e. one

coherent material with two or more metal ions as nodes. The characterization techniques can also shed light onto the distribution

of metal centers, and in many cases it was found that metals are randomly distributed over the nodes. However, the ions sometimes cluster in domains of identical metal nodes, and the presence of this correlated disorder gives rise to new specific properties of the framework. In the field of gas sorption and gas storage, the most important benefit of the MM-MOFs is the way to control the affinity of the MOFs for a certain gas by tuning the metal concentration. This can lead to an enhanced stability (e.g. by rendering the material more hydrophobic or by entering more "noble" metals in the nodes) or to an enhanced affinity. In a similar way, for flexible MOFs their conditions of "breathing" can also be very nicely tuned. In applications such as pressure swing (or temperature swing) adsorption-based processes, this could be an advantage, by controlling the pressure or temperature at which the MOF opens. There are, however, still important questions open in this area, such as understanding the mechanism for breathing in MM-MOFs, and its difference with monometallic materials. It is known, for example in the work on the mixed-metal COMOC-2, that the breathing process is incomplete. Do certain crystals breathe while others do not, or does a crystal breathe "from within"? Would certain domains breathe and others not? If so, what are the conditions to retain crystal integrity? Such open questions could be answered if one would succeed in making a sufficiently large single crystal and studying this during breathing.

In all applications, and certainly in the field of catalysis, the goal is that a MM-MOF should behave distinctly different from just a physical mixture of 2 MOFs. And as always it should be stable enough in the reaction conditions to last a long time. In our honest opinion, this is not necessarily the case in all published studies, where stability control experiments are not systematically performed. Would certain cascade or tandem reactions occur also if the authors would use a physical mixture of monometallic MOFs? This comparison should always be made, otherwise the MM-MOF has no added value. This important point is strongly linked to the question of the catalytic mechanism, which is so important in catalytic studies. The ideal MM-MOF should have a transition state in which the proximity of both metal sites is important to form the intermediate or transition complex. This is rarely shown in literature, and the challenges here are to identify catalytic reactions that really need the proximity of two different metal ions. Inspiration could be found in biochemistry and bimetallic enzymes (e.g. [FeNi]hydrogenase or Acetyl-CoA synthase).

The luminescent applications of MM-MOFs, in particular mixed-lanthanides are also highly interesting. Temperature controlled luminescent materials have, in our opinion, a huge potential in biomedicine, e.g. as thermochromic thermometers capable of measuring local temperature. In such applications however, the cytotoxity of the MOFs could be a serious issue that hampers such developments.

Without reservations, we can conclude that MM-MOFs have shown tremendous potential as smart materials. Huge developments are possible in the field of heterogeneous catalysis, if we can upgrade our applications to true mixed-metal transition state and mimic the bimetallic enzymes. Smart and tunable responses (to gas pressure, to temperature, to pH) makes these materials ever so exciting, and the number of possible applications is probably even larger than our imagination.

We have to see the caveats too: limited stability and leaching of the – often toxic – metals are a few of the possible problems. Another unanswered question is how these MM-MOFs will evolve as a function of time. Will the metal ions diffuse through the framework and form domains anyhow after a period of time? Also, we would call upon the authors to thoroughly study the spent catalysts and report upon the changes in metal distribution, morphology etc. A larger dataset will facilitate researchers to find the necessary trends here. Computational techniques will be of increasing importance in answering such questions.

ASSOCIATED CONTENT

Supporting Information

Table S1 showing the detailed characterization techniques for MM-MOFs, Table S2 literature overview of reported MM-MOFs.

Acknowledgements

The authors thank the support from the Research Board of Ghent University (GOA010-17, GOA2017000303) and the financial support from the Research Foundation Flanders (FWO-Vlaanderen) grant No. G000117N, the latter project was dedicated to MM-MOFs. SA acknowledges the financial support from the Ghent University BOF doctoral grant 01D04318.

References

1. H. Li, M. Eddaoudi, M. O'Keeffe and O. M. Yaghi, *Nature*, 1999, **402**, 276-279.
2. S. Kitagawa and M. Kondo, *B Chem Soc Jpn*, 1998, **71**, 1739-1753.
3. A. K. Cheetham, G. Ferey and T. Loiseau, *Angew Chem Int Edit*, 1999, **38**, 3268-3292.
4. D. Y. Zhao, Q. S. Huo, J. L. Feng, B. F. Chmelka and G. D. Stucky, *J Am Chem Soc*, 1998, **120**, 6024-6036.
5. M. Eddaoudi, J. Kim, N. Rosi, D. Vodak, J. Wachter, M. O'Keeffe and O. M. Yaghi, *Science*, 2002, **295**, 469-472.
6. C. H. Hendon, A. J. Rieth, M. D. Korzynski and M. Dinca, *Acs Central Sci*, 2017, **3**, 554-563.
7. K. Leus, T. Bogaerts, J. De Decker, H. Depauw, K. Hendrickx, H. Vrielinck, V. Van Speybroeck and P. Van Der Voort, *Micropor Mesopor Mat*, 2016, **226**, 110-116.
8. A. Dhakshinamoorthy, A. M. Asiri and H. Garcia, *Catal Sci Technol*, 2016, **6**, 5238-5261.

9. J. Bitzer and W. Kleist, *Chemistry A European Journal*, 2018, DOI: 10.1002/chem.201803887.
10. V. Bernales, M. A. Ortuno, D. G. Truhlar, C. J. Cramer and L. Gagliardi, *Acs Central Sci*, 2018, **4**, 5-19.
11. N. Li, J. Xu, R. Feng, T. L. Hu and X. H. Bu, *Chem Commun*, 2016, **52**, 8501-8513.
12. H. H. Fei and S. M. Cohen, *Chem Commun*, 2014, **50**, 4810-4812.
13. V. Colombo, S. Galli, H. J. Choi, G. D. Han, A. Maspero, G. Palmisano, N. Masciocchi and J. R. Long, *Chem Sci*, 2011, **2**, 1311-1319.
14. R. K. Hocking and T. W. Hambley, *Inorg Chem*, 2003, **42**, 2833-2835.
15. V. M. Goldschmidt, *Trans. Faraday Soc.*, 1929, **25**, 253-283.
16. L. Pauling, *J Am Chem Soc*, 1927, **49**, 765-790.
17. G. Kieslich, S. J. Sun and A. K. Cheetham, *Chem Sci*, 2015, **6**, 3430-3433.
18. W. Travis, E. N. K. Glover, H. Bronstein, D. O. Scanlon and R. G. Palgrave, *Chem Sci*, 2016, **7**, 4548-4556.
19. A. K. Cheetam, G. Kieslich and H. H.-M. Yeung, *Acc. Chem. Res.*, 2018, **51**, 659-667.
20. C. J. Bartel, C. Sutton, B. R. Goldsmith, R. Ouyang, C. B. Musgrave, L. M. Ghiringhelli and M. Sheffler, *Sci. Adv.*, 2019, **5**, eaav0693.
21. M. T. Buscaglia, V. Buscaglia, M. Viviani and P. Nanni, *J Am Ceram Soc*, 2001, **84**, 376-384.
22. G. V. Lewis and C. R. A. Catlow, *J Phys Chem Solids*, 1986, **47**, 89-97.
23. L. J. Wang, H. X. Deng, H. Furukawa, F. Gandara, K. E. Cordova, D. Peri and O. M. Yaghi, *Inorg Chem*, 2014, **53**, 5881-5883.
24. A. K. Cheetham, G. Kieslich and H. H. M. Yeung, *Accounts Chem Res*, 2018, **51**, 659-667.
25. S. Wongsakulphasatch, F. Nouar, J. Rodriguez, L. Scott, C. Le Guillouzer, T. Devic, P. Horcajada, J. M. Greneche, P. L. Llewellyn, A. Vimont, G. Clet, M. Daturi and C. Serre, *Chem Commun*, 2015, **51**, 10194-10197.
26. F. Nouar, T. Devic, H. Chevreau, N. Guillou, E. Gibson, G. Clet, M. Daturi, A. Vimont, J. M. Greneche, M. I. Breeze, R. I. Walton, P. L. Llewellyne and C. Serre, *Chem Commun*, 2012, **48**, 10237-10239.
27. H. Depauw, I. Nevjestic, J. De Winne, G. Wang, K. Haustraete, K. Leus, A. Verberckmoes, C. Detavernier, F. Callens, E. De Canck, H. Vrielinck and P. Van der Voort, *Chem Commun*, 2017, **53**, 8478-8481.
28. Y. Jiao, C. R. Morelock, N. C. Burtch, W. P. Mounfield, J. T. Hungerford and K. S. Walton, *Ind Eng Chem Res*, 2015, **54**, 12408-12414.
29. X. Song, S. Jeong, D. Kim and M. S. Lah, *Crystengcomm*, 2012, **14**, 5753-5756.
30. S. Das, H. Kim and K. Kim, *J Am Chem Soc*, 2009, **131**, 3814-3815.
31. C. K. Brozek and M. Dinca, *J Am Chem Soc*, 2013, **135**, 12886-12891.
32. C. K. Brozek and M. Dinca, *Chem Commun*, 2015, **51**, 11780-11782.
33. H. H. Fei, J. F. Cahill, K. A. Prather and S. M. Cohen, *Inorg Chem*, 2013, **52**, 4011-4016.
34. T. F. Liu, L. F. Zou, D. W. Feng, Y. P. Chen, S. Fordham, X. Wang, Y. Y. Liu and H. C. Zhou, *J Am Chem Soc*, 2014, **136**, 7813-7816.
35. M. Kim, J. F. Cahill, H. H. Fei, K. A. Prather and S. M. Cohen, *J Am Chem Soc*, 2012, **134**, 18082-18088.
36. J. P. Tu, X. L. Zeng, F. J. Xu, X. Wu, Y. F. Tian, X. D. Hou and Z. Long, *Chem Commun*, 2017, **53**, 3361-3364.
37. A. J. Howarth, A. W. Peters, N. A. Vermeulen, T. C. Wang, J. T. Hupp and O. K. Farha, *Chem Mater*, 2017, **29**, 26-39.
38. N. Torres, J. Galicia, Y. Plasencia, A. Cano, F. Echevarria, L. F. Desdin-Garcia and E. Reguera, *Colloid Surface A*, 2018, **549**, 138-146.
39. M. Castellanos and A. R. West, *J Chem Soc Farad T 1*, 1980, **76**, 2159-2169.
40. S. T. Murphy, A. Chroneos, C. Jiang, U. Schwingenschlogl and R. W. Grimes, *Phys Rev B*, 2010, **82**.
41. M. Lammert, C. Glissmann and N. Stock, *Dalton T*, 2017, **46**, 2425-2429.
42. A. F. Sapnik, H. S. Geddes, E. M. Reynolds, H. H. M. Yeung and A. L. Goodwin, *Chem Commun*, 2018, **54**, 9651-9654.
43. Q. X. Yao, J. L. Sun, K. Li, J. Su, M. V. Peskov and X. D. Zou, *Dalton T*, 2012, **41**, 3953-3955.
44. C. K. Brozek, A. F. Cozzolino, S. J. Teat, Y. S. Chen and M. Dinca, *Chem Mater*, 2013, **25**, 2998-3002.
45. C. Castillo-Blas, V. A. de la Pena-O'Shea, I. Puente-Orench, J. R. de Paz, R. Saez-Puche, E. Gutierrez-Puebla, F. Gandara and A. Monge, *Sci Adv*, 2017, **3**.
46. Y. Liu, J. H. Her, A. Dailly, A. J. Ramirez-Cuesta, D. A. Neumann and C. M. Brown, *J Am Chem Soc*, 2008, **130**, 11813-11818.
47. G. Ortiz, G. Chaplais, J. L. Paillaud, H. Nouali, J. Patarin, J. Raya and C. Marichal, *J Phys Chem C*, 2014, **118**, 22021-22029.
48. Z. J. Zhang, L. P. Zhang, L. Wojtas, P. Nugent, M. Eddaoudi and M. J. Zaworotko, *J Am Chem Soc*, 2012, **134**, 924-927.
49. G. P. M. Bignami, Z. H. Davis, D. M. Dawson, S. A. Morris, S. E. Russell, D. McKay, R. E. Parke, D. Iuga, R. E. Morris and S. E. Ashbrook, *Chem Sci*, 2018, **9**, 850-859.
50. O. Kozachuk, M. Meilikhov, K. Yusenko, A. Schneemann, B. Jee, A. V. Kuttatheyil, M. Bertmer, C. Sternemann, A. Poppl and R. A. Fischer, *Eur J Inorg Chem*, 2013, **2013**, 4546-4557.
51. G. Bunker, *Introduction to XAFS : a practical guide to X-ray absorption fine structure spectroscopy*, Cambridge University Press, New York, 2010.
52. J. F. S. do Nascimento, A. M. U. de Araujo, J. Kulesza, A. F. D. Monteiro, S. Alves and B. S. Barros, *New J Chem*, 2018, **42**, 5514-5522.
53. D. Denysenko, T. Werner, M. Grzywa, A. Puls, V. Hagen, G. Eickerling, J. Jelic, K. Reuter and D. Volkmer, *Chem Commun*, 2012, **48**, 1236-1238.
54. A. E. J. Hoffman, L. Vanduyfhuys, I. Nevjestic, J. Wieme, S. M. J. Rogge, H. Depauw, P. Van der Voort, H. Vrielinck and V. Van Speybroeck, *J Phys Chem C*, 2018, **122**, 2734-2746.
55. L. Mitchell, P. Williamson, B. Ehrlichova, A. E. Anderson, V. R. Seymour, S. E. Ashbrook, N. Acerbi, L. M. Daniels, R. I. Walton, M. L. Clarke and P. A. Wright, *Chem-Eur J*, 2014, **20**, 17185-17197.
56. G. de Combarieu, S. Hamelet, F. Millange, M. Morcrette, J. M. Tarascon, G. Ferey and R. I. Walton, *Electrochem Commun*, 2009, **11**, 1881-1884.
57. I. Nevjestic, H. Depauw, P. Gast, P. Tack, D. Deduytsche, K. Leus, M. Van Landeghem, E. Goovaerts, L. Vincze, C. Detavernier, P. Van Der Voort, F. Callens and H. Vrielinck, *Phys Chem Chem Phys*, 2017, **19**, 24545-24554.

58. K. A. Lomachenko, J. Jacobsen, A. L. Bugaev, C. Atzori, F. Bonino, S. Bordiga, N. Stock and C. Lamberti, *J Am Chem Soc*, 2018, **140**, 17379-17383.
59. D. Y. Osadchii, A. I. Olivos-Suarez, A. Szecsenyi, G. N. Li, M. A. Nasalevich, J. A. Dugulan, P. S. Crespo, E. J. M. Hensen, S. L. Veber, M. V. Fedin, G. Sankar, E. A. Pidko and J. Gascon, *Acs Catal*, 2018, **8**, 5542-5548.
60. M. A. Gotthardt, R. Schoch, S. Wolf, M. Bauer and W. Kleist, *Dalton T*, 2015, **44**, 2052-2056.
61. A. Schweiger and G. Jeschke, *Principles of pulse electron paramagnetic resonance*, Oxford University Press, Oxford, 2005.
62. M. Mendt, B. Jee, N. Stock, T. Ahnfeldt, M. Hartmann, D. Himsl and A. Poppl, *J Phys Chem C*, 2010, **114**, 19443-19451.
63. I. Nevjestic, H. Depauw, K. Leus, V. Kalendra, I. Caretti, G. Jeschke, S. Van Doorslaer, F. Callens, P. Van der Voort and H. Vrielinck, *Chemphyschem*, 2015, **16**, 2968-2973.
64. M. Mendt, B. Jee, D. Himsl, L. Moschkowitz, T. Ahnfeldt, N. Stock, M. Hartmann and A. Poppl, *Appl Magn Reson*, 2014, **45**, 269-285.
65. I. Nevjestic, H. Depauw, K. Leus, G. Rampelberg, C. A. Murray, C. Detavernier, P. Van der Voort, F. Callens and H. Vrielinck, *J Phys Chem C*, 2016, **120**, 17400-17407.
66. K. Leus, M. Vandichel, Y. Y. Liu, I. Muylaert, J. Musschoot, S. Pyl, H. Vrielinck, F. Callens, G. B. Marin, C. Detavernier, P. V. Wiper, Y. Z. Khimyak, M. Waroquier, V. Van Speybroeck and P. Van der Voort, *J Catal*, 2012, **285**, 196-207.
67. B. Jee, K. Eisinger, F. Gul-E-Noor, M. Bertmer, M. Hartmann, D. Himsl and A. Poppl, *J Phys Chem C*, 2010, **114**, 16630-16639.
68. S. Friedlander, P. St Petkov, F. Bolling, A. Kultaeva, W. Bohlmann, O. Ovchar, A. G. Belous, T. Heine and A. Poppl, *J Phys Chem C*, 2016, **120**, 27399-27411.
69. M. Simenas, B. Jee, M. Hartmann, J. Banys and A. Poppl, *J Phys Chem C*, 2015, **119**, 28530-28535.
70. H. Depauw, I. Nevjestic, G. B. Wang, K. Leus, F. Callens, E. De Canck, K. De Buysser, H. Vrielinck and P. Van Der Voort, *J Mater Chem A*, 2017, **5**, 24580-24584.
71. Y. Zhang, B. E. G. Lucier, V. V. Terskikh, R. L. Zheng and Y. N. Huang, *Solid State Nucl Mag*, 2017, **84**, 118-131.
72. Q. Liu, H. J. Cong and H. X. Deng, *J Am Chem Soc*, 2016, **138**, 13822-13825.
73. C. Wiktor, M. Meledina, S. Turner, O. I. Lebedev and R. A. Fischer, *J Mater Chem A*, 2017, **5**, 14969-14989.
74. S. O. Odoh, C. J. Cramer, D. G. Truhlar and L. Gagliardi, *Chem Rev*, 2015, **115**, 6051-6111.
75. J. D. Evans, G. Fraux, R. Gaillac, D. Kohen, F. Trousselet, J. M. Vanson and F. X. Coudert, *Chem Mater*, 2017, **29**, 199-212.
76. T. D. Bennett, A. K. Cheetham, A. H. Fuchs and F. X. Coudert, *Nat Chem*, 2017, **9**, 11-16.
77. M. Fuentes-Cabrera, D. M. Nicholson, B. G. Sumpter and M. Widom, *J Chem Phys*, 2005, **123**.
78. L. M. Yang, P. Vajeeston, P. Ravindran, H. Fjellvag and M. Tilset, *Phys Chem Chem Phys*, 2011, **13**, 10191-10203.
79. E. A. Dolgopolova, A. J. Brandt, O. A. Ejegbavwo, A. S. Duke, T. D. Maddumapatabandi, R. P. Galhenage, B. W. Larson, O. G. Reid, S. C. Ammal, A. Heyden, M. Chandrashekhar, V. Stavila, D. A. Chen and N. B. Shustova, *J Am Chem Soc*, 2017, **139**, 5201-5209.
80. B. Mandal, J. S. Chung and S. G. Kang, *Phys Chem Chem Phys*, 2017, **19**, 31316-31324.
81. D. R. Sun, W. J. Liu, M. Qiu, Y. F. Zhang and Z. H. Li, *Chem Commun*, 2015, **51**, 2056-2059.
82. C. H. Lau, R. Babarao and M. R. Hill, *Chem Commun*, 2013, **49**, 3634-3636.
83. X. L. Liu, G. H. Chen, X. J. Wang, P. Li, Y. B. Song and R. Y. Li, *Phys Chem Chem Phys*, 2017, **19**, 29963-29974.
84. D. Denysenko, J. Jelic, K. Reuter and D. Volkmer, *Chem-Eur J*, 2015, **21**, 8188-8199.
85. X. L. Wang, L. Z. Dong, M. Qiao, Y. J. Tang, J. Liu, Y. F. Li, S. L. Li, J. X. Su and Y. Q. Lan, *Angew Chem Int Edit*, 2018, **57**, 9660-9664.
86. D. R. Pahls, M. A. Ortuno, P. H. Winegar, C. J. Cramer and L. Gagliardi, *Inorg Chem*, 2017, **56**, 8739-8743.
87. A. Benali, Y. Luo, H. Shin, D. Pahls and O. Heinonen, *J Phys Chem C*, 2018, **122**, 16683-16691.
88. A. K. Cheetham, T. D. Bennett, F. X. Coudert and A. L. Goodwin, *Dalton T*, 2016, **45**, 4113-4126.
89. M. J. Cliffe, W. Wan, X. D. Zou, P. A. Chater, A. K. Kleppe, M. G. Tucker, H. Wilhelm, N. P. Funnell, F. X. Coudert and A. L. Goodwin, *Nat Commun*, 2014, **5**.
90. M. J. Cliffe, J. A. Hill, C. A. Murray, F. X. Coudert and A. L. Goodwin, *Phys Chem Chem Phys*, 2015, **17**, 11586-11592.
91. F. Trousselet, A. Archereau, A. Boutin and F. X. Coudert, *J Phys Chem C*, 2016, **120**, 24885-24894.
92. C. Castillo-Blas and F. Gandara, *Israel Journal of Chemistry*, 2018, **58**, 1036-1043.
93. J. D. Howe, C. R. Morelock, Y. Jiao, K. W. Chapman, K. S. Walton and D. S. Sholl, *J Phys Chem C*, 2017, **121**, 627-635.
94. R. M. Marti, J. D. Howe, C. R. Morelock, M. S. Conradi, K. S. Walton, D. S. Sholl and S. E. Hayes, *J Phys Chem C*, 2017, **121**, 25778-25787.
95. Y. B. Huang, J. Liang, X. S. Wang and R. Cao, *Chem Soc Rev*, 2017, **46**, 126-157.
96. S. Abednatanzi, K. Leus, P. G. Derakhshandeh, F. Nahra, K. De Keukeleere, K. Van Hecke, I. Van Driessche, A. Abbasi, S. P. Nolan and P. Van Der Voort, *Catal Sci Technol*, 2017, **7**, 1478-1487.
97. S. Abednatanzi, P. G. Derakhshandeh, A. Abbasi, P. Van der Voort and K. Leus, *Chemcatchem*, 2016, **8**, 3672-3679.
98. H. H. Kung, *Transition Metal Oxides: Surface Chemistry and Catalysis*, Elsevier, Amsterdam, The Netherlands 1989.
99. J. Hagen, *Industrial catalysis : a practical approach*, Wiley-VCH, Weinheim, 2006.
100. K. Weissermel and H.-J. r. Arpe, *Industrial organic chemistry*, Wiley-VCH, Weinheim; New York; Basel; Cambridge, 1993.
101. C. Parmeggiani, C. Matassini and F. Cardona, *Green Chem*, 2017, **19**, 2030-2050.
102. D. R. Sun, F. X. Sun, X. Y. Deng and Z. H. Li, *Inorg Chem*, 2015, **54**, 8639-8643.
103. Y. H. Fu, L. Xu, H. M. Shen, H. Yang, F. M. Zhang, W. D. Zhu and M. H. Fan, *Chem Eng J*, 2016, **299**, 135-141.
104. M. Amini, M. M. Haghdoost and M. Bagherzadeh, *Coordin Chem Rev*, 2013, **257**, 1093-1121.
105. M. N. Timofeeva, V. N. Panchenko, N. A. Khan, Z. Hasan, I. P. Prosvirin, S. V. Tsybulya and S. H. Jhung, *Appl Catal a-Gen*, 2017, **529**, 167-174.
106. D. Sahap, D. K. Hazra, T. Maity and S. Koner, *Inorg Chem*, 2016, **55**, 5729-5731.

107. F. Nouar, M. I. Breeze, B. C. Campo, A. Vimont, G. Clet, M. Daturi, T. Devic, R. I. Walton and C. Serre, *Chem Commun*, 2015, **51**, 14458-14461.
108. M. C. Wen, Y. Kuwahara, K. Mori, D. Q. Zhang, H. X. Li and H. Yamashita, *J Mater Chem A*, 2015, **3**, 14134-14141.
109. A. Schejn, A. Aboulaich, L. Balan, V. Falk, J. Lalevee, G. Medjahdi, L. Aranda, K. Mozet and R. Schneider, *Catal Sci Technol*, 2015, **5**, 1829-1839.
110. A. Abbasi, M. Soleimani, M. Najafi and S. Geranmayeh, *Inorg Chim Acta*, 2016, **439**, 18-23.
111. C. P. Krap, R. Newby, A. Dhakshinamoorthy, H. Garcia, I. Cebula, T. L. Easun, M. Savage, J. E. Eyley, S. Gao, A. J. Blake, W. Lewis, P. H. Beton, M. R. Warren, D. R. Allan, M. D. Frogley, C. C. Tang, G. Cinque, S. H. Yang and M. Schroder, *Inorg Chem*, 2016, **55**, 1076-1088.
112. T. K. Pal, D. De, S. Neogi, P. Pachfule, S. Senthilkumar, Q. Xu and P. K. Bharadwaj, *Chem-Eur J*, 2015, **21**, 19064-19070.
113. L. M. Aguirre-Diaz, F. Gandara, M. Iglesias, N. Snejko, E. Gutierrez-Puebla and M. A. Monge, *J Am Chem Soc*, 2015, **137**, 6132-6135.
114. C. M. Zhao, X. Y. Dai, T. Yao, W. X. Chen, X. Q. Wang, J. Wang, J. Yang, S. Q. Wei, Y. E. Wu and Y. D. Li, *J Am Chem Soc*, 2017, **139**, 8078-8081.
115. Y. Lee, S. Kim, J. K. Kang and S. M. Cohen, *Chem Commun*, 2015, **51**, 5735-5738.
116. R. N. Amador, M. Carboni and D. Meyer, *Rsc Adv*, 2017, **7**, 195-200.
117. A. M. Rasero-Almansa, M. Iglesias and F. Sanchez, *Rsc Adv*, 2016, **6**, 106790-106797.
118. T. A. Vu, G. H. Le, C. D. Dao, L. Q. Dang, K. T. Nguyen, P. T. Dang, H. T. K. Tran, Q. T. Duong, T. V. Nguyen and G. D. Lee, *Rsc Adv*, 2014, **4**, 41185-41194.
119. X. S. Wang, M. Chrzanowski, L. Wojtas, Y. S. Chen and S. Ma, *Chem-Eur J*, 2013, **19**, 12187-12187.
120. M. Dan-Hardi, C. Serre, T. Frot, L. Rozes, G. Maurin, C. Sanchez and G. Ferey, *J Am Chem Soc*, 2009, **131**, 10857-10859.
121. K. Hendrickx, J. J. Joos, A. De Vos, D. Poelman, P. F. Smet, V. Van Speybroeck, P. Van Der Voort and K. Lejaeghere, *Inorg Chem*, 2018, **57**, 5463-5474.
122. X. P. Wu, L. Gagliardi and D. G. Truhlar, *J Chem Phys*, 2019, **150**.
123. Q. G. Zhai, X. H. Bu, C. Y. Mao, X. Zhao and P. Y. Feng, *J Am Chem Soc*, 2016, **138**, 2524-2527.
124. J. A. Botas, G. Calleja, M. Sanchez-Sanchez and M. G. Orcajo, *Langmuir*, 2010, **26**, 5300-5303.
125. Z. Y. Zhou, L. Mei, C. Ma, F. Xu, J. Xiao, Q. B. Xia and Z. Li, *Chem Eng Sci*, 2016, **147**, 109-117.
126. J. A. Botas, G. Calleja, M. Sanchez-Sanchez and M. G. Orcajo, *Int J Hydrogen Energ*, 2011, **36**, 10834-10844.
127. J. A. Villajos, G. Orcajo, C. Martos, J. A. Botas, J. Villacanas and G. Calleja, *Int J Hydrogen Energ*, 2015, **40**, 5346-5352.
128. K. Hong, W. Bak, D. Moon and H. Chun, *Cryst Growth Des*, 2013, **13**, 4066-4070.
129. X. Song, M. Oh and M. S. Lah, *Inorg Chem*, 2013, **52**, 10869-10876.
130. Z. W. Wei, W. G. Lu, H. L. Jiang and H. C. Zhou, *Inorg Chem*, 2013, **52**, 1164-1166.
131. S. T. Zheng, T. Wu, C. T. Chou, A. Fuhr, P. Y. Feng and X. H. Bu, *J Am Chem Soc*, 2012, **134**, 4517-4520.
132. M. Dinca and J. R. Long, *J Am Chem Soc*, 2007, **129**, 11172-11176.
133. G. Kaur, R. K. Rai, D. Tyagi, X. Yao, P. Z. Li, X. C. Yang, Y. L. Zhao, Q. Xu and S. K. Singh, *J Mater Chem A*, 2016, **4**, 14932-14938.
134. J. H. Liao, W. T. Chen, C. S. Tsai and C. C. Wang, *Crystengcomm*, 2013, **15**, 3377-3384.
135. K. Hong, W. Bak and H. Chun, *Inorg Chem*, 2013, **52**, 5645-5647.
136. S. J. D. Smith, B. P. Ladewig, A. J. Hill, C. H. Lau and M. R. Hill, *Sci Rep-Uk*, 2015, **5**.
137. J. Ferrando-Soria, P. Serra-Crespo, M. de Lange, J. Gascon, F. Kapteijn, M. Julve, J. Cano, F. Lloret, J. Pasan, C. Ruiz-Perez, Y. Journaux and E. Pardo, *J Am Chem Soc*, 2012, **134**, 15301-15304.
138. Y. Cao, Y. X. Zhao, F. J. Song and Q. Zhong, *J Energy Chem*, 2014, **23**, 468-474.
139. S. R. Caskey, A. G. Wong-Foy and A. J. Matzger, *J Am Chem Soc*, 2008, **130**, 10870-10871.
140. W. L. Queen, M. R. Hudson, E. D. Bloch, J. A. Mason, M. I. Gonzalez, J. S. Lee, D. Gygi, J. D. Howe, K. Lee, T. A. Darwish, M. James, V. K. Peterson, S. J. Teat, B. Smit, J. B. Neaton, J. R. Long and C. M. Brown, *Chem Sci*, 2014, **5**, 4569-4581.
141. J. A. Mason, K. Sumida, Z. R. Herm, R. Krishna and J. R. Long, *Energ Environ Sci*, 2011, **4**, 3030-3040.
142. D. Britt, H. Furukawa, B. Wang, T. G. Glover and O. M. Yaghi, *P Natl Acad Sci USA*, 2009, **106**, 20637-20640.
143. K. Sumida, D. L. Rogow, J. A. Mason, T. M. McDonald, E. D. Bloch, Z. R. Herm, T. H. Bae and J. R. Long, *Chem Rev*, 2012, **112**, 724-781.
144. Y. Y. Liu, S. Couck, M. Vandichel, M. Grzywa, K. Leus, S. Biswas, D. Vollmer, J. Gascon, F. Kapteijn, J. F. M. Denayer, M. Waroquier, V. Van Speybroeck and P. Van der Voort, *Inorg Chem*, 2013, **52**, 113-120.
145. Y. J. Cui, H. Xu, Y. F. Yue, Z. Y. Guo, J. C. Yu, Z. X. Chen, J. K. Gao, Y. Yang, G. D. Qian and B. L. Chen, *J Am Chem Soc*, 2012, **134**, 3979-3982.
146. X. T. Rao, T. Song, J. K. Gao, Y. J. Cui, Y. Yang, C. D. Wu, B. L. Chen and G. D. Qian, *J Am Chem Soc*, 2013, **135**, 15559-15564.
147. A. Cadiau, C. D. S. Brites, P. M. F. J. Costa, R. A. S. Ferreira, J. Rocha and L. D. Carlos, *Acs Nano*, 2013, **7**, 7213-7218.
148. X. S. Lian, D. Zhao, Y. J. Cui, Y. Yang and G. D. Qian, *Chem Commun*, 2015, **51**, 17676-17679.
149. Z. P. Wang, D. Ananias, A. Carne-Sanchez, C. D. S. Brites, I. Imaz, D. Maspoch, J. Rocha and L. D. Carlos, *Adv Funct Mater*, 2015, **25**, 2824-2830.
150. D. A. Zhao, D. Yue, L. Zhang, K. Jiang and G. D. Qian, *Inorg Chem*, 2018, **57**, 12596-12602.
151. L. Li, J. H. Cheng, Z. P. Liu, L. Song, Y. J. You, X. H. Zhou and W. Huang, *Acs Appl Mater Inter*, 2018, **10**, 44109-44115.
152. D. K. Singha, S. Bhattacharya, P. Majee, S. K. Mondal, M. Kumar and P. Mahata, *J Mater Chem A*, 2014, **2**, 20908-20915.
153. D. K. Singha, P. Majee, S. K. Mondal and P. Mahata, *Eur J Inorg Chem*, 2015, DOI: 10.1002/ejic.201403097, 1390-1397.
154. K. A. White, D. A. Chengelis, K. A. Gogick, J. Stehman, N. L. Rosi and S. Petoud, *J Am Chem Soc*, 2009, **131**, 18069-18071.
155. S. N. Zhao, G. B. Wang, D. Poelman and P. Van der Voort, *Materials*, 2018, **11**.